

RESEARCH ARTICLE

10.1002/2016JC012613

Key Points:

- Sea-surface temperature anomalies during wind relaxation are of order 1°C and extend 2000 km offshore
- Atmosphere-ocean heat flux drives the northern relaxation SST anomalies via reduced latent cooling
- During southern relaxations, preconditioned cold water and more clouds offset reduced latent cooling

Correspondence to:

M. Fewings,
melanie.fewings@uconn.edu

Citation:

Flynn, K. R., M. R. Fewings, C. Gotschalk, and K. Lombardo (2017), Large-scale anomalies in sea-surface temperature and air-sea fluxes during wind relaxation events off the United States West Coast in summer, *J. Geophys. Res. Oceans*, 122, doi:10.1002/2016JC012613.

Received 8 DEC 2016

Accepted 1 MAR 2017

Accepted article online 7 MAR 2017

Large-scale anomalies in sea-surface temperature and air-sea fluxes during wind relaxation events off the United States West Coast in summer

Kayla R. Flynn^{1,2} , Melanie R. Fewings¹ , Christopher Gotschalk³ , and Kelly Lombardo¹ 

¹Department of Marine Sciences, University of Connecticut, Groton, Connecticut, USA, ²Now at NASA Goddard Institute for Space Studies and Trinnovim, LLC, New York, New York, USA, ³Marine Science Institute, University of California, Santa Barbara, California, USA

Abstract In summertime along the U.S. West Coast, the winds exhibit a three-stage cycle spanning ~12 days. The prevailing upwelling-favorable winds weaken (relax) or reverse off the Pacific Northwest, then reintensify, then weaken off central California. We study the sea-surface temperature (SST) response to these “northern” and “southern” wind relaxations. (1) Satellite data indicate northern wind relaxations result in SST anomalies $O(+1^\circ\text{C})$ extending ~2000 km offshore. Surface heat flux reanalyses indicate the warm anomaly is mainly from decreased latent cooling. (2) After the winds reintensify, SST becomes anomalously cold along central and southern California. (3) During the southern wind relaxations, the cold SST anomaly persists but the SST warms with time. This warming is not driven by surface heat flux. The latent cooling is reduced, yet unlike during the northern relaxation, this change is canceled by a decrease in solar radiation due to increased cloudiness. In the region south of Point Conception, reduced southward advection of cold water and increased northward advection of warm water by the coastal countercurrent could explain the warming. Reduced Ekman pumping likely contributes to the warming trend during the southern relaxations, and reduced wind-driven entrainment at the base of the mixed layer likely contributes to the warming during both relaxations. Whether the net surface heat flux is the main driver of SST anomalies during wind relaxation depends on the regional response of clouds. Southern wind relaxations follow episodes of enhanced surface cooling, which may contribute to greater cloudiness during southern than northern wind relaxations.

Plain Language Summary In summertime along the United States West Coast, the winds exhibit a 3-stage cycle spanning ~12 days. The prevailing southward winds weaken (relax) or reverse off the Pacific Northwest, then reintensify, then weaken off central and southern California. This leads to variability in the strength of wind-driven coastal upwelling of cold, nutrient-rich ocean water that fuels economically important fisheries. In a previous paper, we studied the atmospheric pressure patterns that force that wind event cycle. Here, we use satellite data to study the sea-surface temperature (SST) response to the northern and southern (Pacific Northwest vs. central California) wind relaxations. We find that 1) the 3-stage wind event cycle creates substantial SST anomalies extending ~2000 km offshore, 2) the heat exchange between the atmosphere and ocean during these events is different in the northern vs. southern wind relaxations due to differences in cloud cover, and 3) the wind intensification (stage 2 of the event cycle) preconditions the SST to be cold before the southern relaxations, preventing the expected warm SST anomaly from developing during the subsequent relaxation and possibly contributing to the greater cloud cover observed during southern relaxations, which has implications for human mortality during California heat waves.

1. Introduction

1.1. Upwelling-Favorable Wind Stress and Wind Relaxations

Wind-driven coastal upwelling occurs globally in eastern boundary current systems. The upwelled water is typically cold and nutrient-rich and fuels high oceanic productivity. As a result, eastern boundary current systems represent ~1% of the global ocean by surface area, but yield more than 20% of all wild-marine-captured fish, and are essential ecosystems for marine biodiversity [Dudas *et al.*, 2009; Iles *et al.*, 2012; Morgan *et al.*, 2012]. However, in many locations, the upwelling-favorable wind that drives this productivity

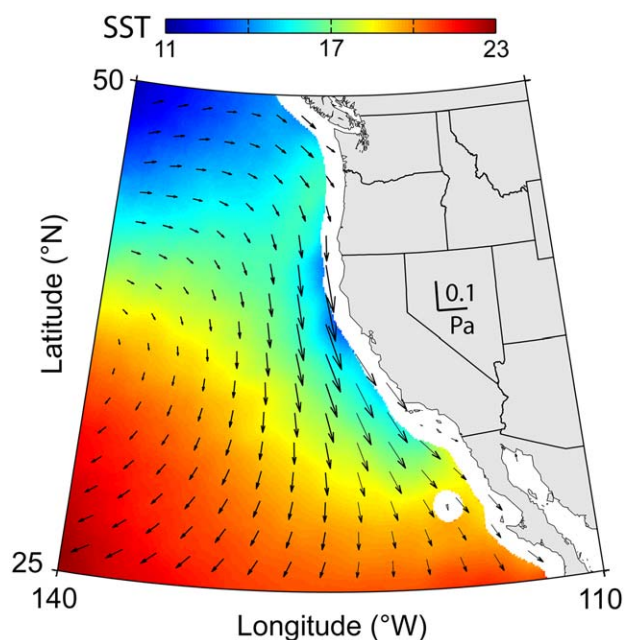


Figure 1. Mean SST and wind stress in summer off the west coast of North America. Color: mean SST ($^{\circ}\text{C}$) from AMSR-E during June–August 2002–2009. Arrows: mean wind stress from QuikSCAT satellite (subsampling) as in *Fewings et al.* [2016]. Arrow length indicates wind stress magnitude according to the scale over land. White area along the coast indicates insufficient AMSR-E data.

upwelling-favorable winds that lasts for several days [e.g., *Kosro*, 1987]. The duration of these events is typically 2–5 days [e.g., *Bane et al.*, 2005; *Melton et al.*, 2009]. Some relaxation events develop into wind reversals, resulting in downwelling-favorable winds [e.g., *Bond et al.*, 1996; *Mass and Bond*, 1996; *Nuss et al.*, 2000; *Nuss*, 2007].

The wind relaxations and reversals in the northern and southern parts of the CCS are linked through the midlevel atmospheric forcing. *Halliwel and Allen* [1987] coined the term “event cycle” to refer to repeated, alternating events in summer in which a wind relaxation or reversal occurs in the poleward part of the CCS and then the winds intensify off northern California. These event cycles are caused by a midlevel trough, followed by a midlevel ridge, both detectable at the 500 hPa level; the associated sealevel pressure (SLP) anomalies drive the northern wind relaxation and the reintensification [*Halliwel and Allen*, 1987; *Mass and Bond*, 1996]. The two 500 hPa height anomalies constitute the entire event cycle at midlevel in the atmosphere. At sea level, however, there is a third stage in the cycle [*Fewings et al.*, 2016]. The anticyclonic atmospheric circulation associated with the midlevel ridging, essentially a northeastward extension of the North Pacific High atmospheric pressure system, advects warm air offshore from the desert in the southwestern U.S., causing a low-pressure anomaly at sea level [*Nuss*, 2007]. The along-coast pressure gradient forces associated with this second low SLP anomaly both increase the wind reintensification in the northern CCS and drive the southern wind relaxation [*Fewings et al.*, 2016] or rarer reversal [*Nuss*, 2007]. The entire three-stage “event cycle” lasts ~ 12 days on average [*Fewings et al.*, 2016].

1.2. Ocean and Atmosphere Response to Wind Relaxation in the CCS

The literature on the oceanic response to wind relaxation and reversal in the CCS focuses on the area within tens of kilometers of the coast. There are changes to circulation and stratification [*Harms and Winant*, 1998; *Gan and Allen*, 2002; *Winant et al.*, 2003; *Dever*, 2004; *Kirincich and Barth*, 2009; *Fewings et al.*, 2015], changes to larval transport [*Dudas et al.*, 2009; *Iles et al.*, 2012; *Morgan et al.*, 2012], and warm poleward ocean flows [*Send et al.*, 1987; *Melton et al.*, 2009; *Washburn et al.*, 2011; *Suanda et al.*, 2016]. In addition, wind relaxations are important for marine weather forecasts due to the effect on cloudiness. Low marine stratus clouds generally form during the southern wind relaxations [*Kosro*, 1987; *Rahn and Parish*, 2010]. The low marine clouds reduce solar heating, resulting in colder than normal SSTs. Cold SSTs can in turn further intensify the atmospheric boundary layer temperature inversion, reinforcing the low marine clouds [e.g., *Wang et al.*,

displays episodic weakening, or relaxation, and occasionally reverses direction for several days. This occurs in all the major eastern boundary current systems, including the Canary Current upwelling system [*Relvas and Barton*, 2002, 2005; *García-Lafuente et al.*, 2006]; the Benguela Current System at Cape Columbine, South Africa [*Fawcett et al.*, 2008]; the Chile-Peru System [*Strub et al.*, 1998; *Garreaud et al.*, 2002]; and the California Current System (CCS) [*Send et al.*, 1987; *Bond et al.*, 1996; *Mass and Bond*, 1996; *Harms and Winant*, 1998; *Winant et al.*, 2003; *Bane et al.*, 2005, 2007; *Melton et al.*, 2009; *Washburn et al.*, 2011].

The CCS extends along the United States (U.S.) West Coast from Washington to California [*Hickey*, 1979; *Lynn and Simpson*, 1987]. The mean wind over the CCS in summer is upwelling favorable (Figure 1), but wind relaxations occur ~ 1 –2 times per month [*Halliwel and Allen*, 1987; *Bond et al.*, 1996; *Melton et al.*, 2009]. The definition of a wind relaxation is a calming in

2004]. Increased inversion strength is known to be associated with increased occurrence of marine stratus [e.g., Wood and Bretherton, 2006] (reviewed in Wood [2012]), including off California [Jacobellis and Cayan, 2013].

A recent study using satellite vector wind stress composites indicates the wind stress anomalies during these relaxations extend >1000 km offshore [Fewings *et al.*, 2016]. That leads to the question: how do these synoptic-scale wind relaxations change SST during the “event cycle” described in section 1.1? The wind stress affects the net surface heat flux, an important driver of changes in SST. Evaporation, which leads to latent cooling, increases with wind stress [e.g., Edson *et al.*, 2013]. The clouds associated with wind relaxation will reduce the shortwave radiation. The wind stress also drives ocean currents that lead to horizontal advection and diffusion of SST variations, and shear-driven mixing that results in entrainment of deeper, colder water to the surface mixed layer. Curl in the wind stress can result in divergence in the surface waters [e.g., Cronin and Sprintall, 2009], producing upwelling of cold water. Therefore, the changes in wind stress during the three-stage event cycle should lead to changes in SST by multiple mechanisms. The present study focuses on the impact of the CCS wind relaxations on SST and atmosphere-ocean heat fluxes on scales of 100–2000 km offshore.

1.3. Purpose of This Study

The purpose of this study is to determine the regional SST response to wind relaxations along the U.S. West Coast, and the causes of the SST response, through an analysis of satellite SST data and surface heat fluxes from reanalyses. We focus on June–August 2002–2009 based on satellite data availability. The study domain is the same as in Fewings *et al.* [2016] (Figure 1). We focus on temperature changes in the ocean surface mixed layer (ML) on time scales of hours to days, and analyze the SST response to wind relaxations by using a time-integrated ML heat budget. Our three questions addressed in this analysis are: (1) What SST anomalies are associated with the wind relaxation patterns? (2) Are anomalies in the surface heat flux the main driver of the SST anomalies? and (3) Which surface heat flux components are the main contributors to the net surface heat flux anomalies?

Section 2 describes the 3-D heat budget setup; the components of the net surface heat flux; the satellite and reanalysis products; the wind stress curl and MLD calculations; the Argo float data; and how we constructed composite anomalies based on the wind events. Section 3 describes the evolution of the composite SST and surface heat flux anomalies during the 12 day wind event cycle and the relative sizes of the surface heat flux components. In section 4, we discuss the main drivers of the SST anomalies during the northern versus southern wind relaxations, the possible role of wind stress-SST feedbacks, and the connection to observed regional weather, particularly clouds. Section 5 summarizes our study.

2. Data and Methods

2.1. Satellite SST

To determine the SST response to wind relaxations, we use data from a satellite-borne microwave radiometer. The National Aeronautics and Space Administration (NASA) Advanced Microwave Scanning Radiometer-Earth Observing System (AMSR-E) on the polar-orbiting Aqua satellite collected SST data from 2002 to 2011. AMSR-E covered 89% of the globe daily with a resolution of ~56 km. The AMSR-E data exclude rain-contaminated measurements but not cloudy conditions, so the data availability is about 95% [Chelton and Wentz, 2005]. In contrast, with the higher-resolution thermal infrared satellite SST sensors such as the Advanced Very High Resolution Radiometer (AVHRR) that exclude cloudy conditions, coverage drops to less than 30% [Chelton *et al.*, 2007]. Therefore, using a microwave radiometer is advantageous here because it can sample through clouds [Wentz *et al.*, 2000], which are common over the CCS in summer (section 1.2). We used the Group for High-Resolution Sea Surface Temperature Level 2P swath product [Remote Sensing Systems, 2004]. We linearly interpolated the AMSR-E data onto a regular 0.1° latitude-longitude grid.

2.2. Mixed-Layer Heat Budget

Changes to ML ocean temperature can result from many processes, so we use a heat budget as a tool to diagnose which processes are the most important during wind relaxations. We assume that temperature is uniform from the surface to the base of the ML and use SST as a proxy for ML temperature. Though satellite SST is not exactly equivalent to vertically averaged ML temperature, this assumption is reasonable given the

uncertainty in the data products. The vertically integrated heat budget for the ML used here is similar to *Stevenson and Niiler* [1983] and *Moisan and Niiler* [1998] but with the horizontal eddy diffusion term retained:

$$\frac{\partial SST}{\partial t} = \underbrace{\frac{Q_{net}}{\rho_w c_p h}}_A - \underbrace{\frac{SWR_{-h}}{\rho_w c_p h}}_B - \underbrace{\tilde{u} \cdot \nabla_H SST}_C - \underbrace{\kappa_H \nabla_H^2 SST}_D - \underbrace{\frac{(SST - T_{-h})}{h} \left(\frac{\partial h}{\partial t} + \tilde{u}_{-h} \cdot \nabla_H h + w_{-h} \right)}_E - \underbrace{\frac{1}{h} \nabla_H \cdot \int_{-h}^0 \tilde{u} \tilde{SST} dz}_F \quad (1)$$

where SWR_{-h} is the shortwave radiation (SWR) penetrating past the ML base at $z = -h$, $z = 0$ at the mean sea surface, t is time, ρ_w is seawater density, and c_p is the specific heat capacity of seawater. The horizontal water velocity is \tilde{u} . The horizontal gradient operator is ∇_H , κ_H is the horizontal eddy diffusivity, T_{-h} is the temperature just below the base of the ML, and w_{-h} is the vertical velocity at the base of the ML. Tilde ($\tilde{}$) indicates a vertical average over the mixed layer has been removed. The left side of equation (1) represents the temperature trend. Term A contains the net surface heat flux (defined below in section 2.3, equation (7)). Term B is the penetrating radiation, which is absorbed below the mixed layer. Term C is horizontal advection of SST gradients by geostrophic currents, Ekman flow, and other surface currents. Term D is horizontal eddy diffusion of SST gradients. Term E represents SST changes due to ML entrainment or detrainment, mixing of water into the ML from below. Entrainment is written here as the change in mixed-layer depth (MLD) h (i.e., the part of $\partial h / \partial t$) that is not due simply to horizontal advection of spatial variations in MLD ($\tilde{u}_{-h} \cdot \nabla_H h$) or vertical advection at the base of the ML (w_{-h}). If there is no entrainment, then h is a material surface and the horizontal advective changes in h are balanced by the vertical motion of the base of the mixed layer and the change in h with time, based on conservation of mass. This movement of h as a material surface includes Ekman pumping due to wind stress curl, which does not directly result in changes in ML temperature or SST where isotherms are not outcropping. Changes in SST result from the remainder of $\partial h / \partial t$, which is due to vertical entrainment (e.g., from shear-driven vertical mixing at the base of the mixed layer). Term F is the covariance between \tilde{u} , the deviation from the vertically averaged horizontal velocity within the ML, and \tilde{SST} , the deviation from the vertically averaged temperature. Below, we ignore the covariance term, F, because we assume the ML is completely mixed in both temperature and velocity.

To determine what part of the SST changes can be explained by changes in surface heat flux, we use a time-integrated version of the heat budget in equation (1). We simplify the time integral of equation (1) to test a 1-D heat budget:

$$SST(t) - SST(t_0) - \int_{t_0}^t \frac{Q_{net}}{\rho_w c_p h} dt = \int_{t_0}^t R dt \quad (2)$$

where we combine terms B, C, D, and E from equation (1) into a residual: $R \equiv B + C + D + E$, and neglect term F as stated above. SST is the SST at time t , and t_0 is a reference time (e.g., the start of the wind relaxation; see section 2.7). The MLD, h , is held constant at the summer climatological spatial mean value of the MLD (section 2.5). We refer to the terms on the left-hand side of equation (2) as ΔSST_{Obs} and $\Delta SST_{Q_{net}}$ respectively, where

$$\Delta SST_{Obs} \equiv SST(t) - SST(t_0) \quad (3)$$

is the observed change in SST and

$$\Delta SST_{Q_{net}} \equiv \int_{t_0}^t \frac{Q_{net}}{\rho_w c_p h} dt \quad (4)$$

is the predicted change in SST if Q_{net} is the sole driver of ML temperature. The right-hand side of equation (2) is ΔSST_{Res} :

$$\Delta SST_{Res} \equiv \int_{t_0}^t R dt \quad (5)$$

where ΔSST_{Res} is the inferred change in SST from the remaining heat budget terms (B, C, D, and E in equation (1)). Then the full budget is

$$\Delta SST_{Obs} - \Delta SST_{Q_{net}} = \Delta SST_{Res} \quad (6)$$

If surface heat flux is the sole driver of changes in SST, then $\Delta SST_{Res} = 0$.

2.3. Components of the Surface Heat Flux: OAFflux and ISCCP

Here, the sign convention is that a downward heat flux from atmosphere to ocean is positive, indicating ocean warming. The net surface heat flux, Q_{net} , is the sum of four component fluxes: net shortwave radiation Q_{SWR} , net longwave radiation Q_{LWR} , sensible heat flux Q_{SHF} , and latent heat flux Q_{LHF} , so that

$$Q_{net} = Q_{SWR} + Q_{LWR} + Q_{SHF} + Q_{LHF} \quad (7)$$

For the sensible and latent heat fluxes, we use the Objectively Analyzed Air-sea Fluxes (OAFflux) product [Yu and Weller, 2007; Yu et al., 2008]. OAFflux is a global product produced by an optimal blending of multiplatform satellite retrievals with three numerical weather prediction reanalyses. Comparison with buoy data determines the weight of each reanalysis and satellite product. OAFflux uses the COARE 3.0 bulk algorithm [Edson et al., 2013] to calculate SHF and LHF. Gap-free SHF and LHF, as well as wind velocity and SST, are provided daily from 1985 to present on a 1° latitude-longitude grid.

The net incoming shortwave radiation is [e.g., Yu and Weller, 2007]:

$$Q_{SWR} = SWR_d - SWR_u = (1 - \alpha)SWR_d \quad (8)$$

where SWR_d is the downward SWR into the ocean and α is the ocean surface albedo, which depends mainly on solar elevation angle and cloud cover [e.g., Payne, 1972]. SWR entering the ocean is absorbed over depths of tens of meters, so some SWR may penetrate through the bottom of the mixed layer, represented by term B in equation (1).

The net LWR at the ocean surface, Q_{LWR} , can be split into downwelling LWR (LWR_d) and upwelling LWR (LWR_u). LWR_u is the sum of black-body radiation emitted from the ocean and the fraction $1 - \epsilon$ of downwelling LWR reflected by the ocean surface:

$$LWR_u = \epsilon \sigma T_s^4 + (1 - \epsilon)LWR_d \quad (9)$$

where $\epsilon = 0.97$ is the infrared emissivity of the ocean surface, σ is the Stefan-Boltzmann constant, and T_s is the ocean surface skin temperature [e.g., Fairall et al., 1996]. Then the net LWR is

$$Q_{LWR} = LWR_d - LWR_u = \epsilon LWR_d - \epsilon \sigma T_s^4 \quad (10)$$

The shortwave and longwave radiative fluxes used here are provided with OAFflux on the same space-time grid as SHF and LHF, but come from the International Satellite Cloud Climatology Project (ISCCP) [Schiffer and Rossow, 1983]. ISCCP radiative fluxes are computed by a radiative transfer model from the Goddard Institute for Space Studies (GISS) General Circulation Model (GCM). Global ISCCP fluxes for clear and cloudy skies are available every 3 h on a 2.5° latitude-longitude grid. For consistency, OAFflux provides daily ISCCP fluxes linearly interpolated onto the 1° OAFflux grid. Further detail can be found in Yu et al. [2008] or Flynn [2016, Appendix]. The uncertainty in the ISCCP shortwave and longwave fluxes on monthly mean time scales (an appropriate comparison since we average over many synoptic events) is $\sim 10\text{--}15 \text{ W m}^{-2}$ [Rossow and Zhang, 1995; Zhang et al., 2004]. Together, OAFflux and ISCCP provide this study with daily estimates of Q_{net} , SHF, LHF, SWR, LWR, SST, and wind velocity.

2.4. SST From AMSR-E Versus OAFflux

Although we use the AMSR-E satellite data to characterize the SST anomalies (section 2.1), in the heat budget analysis we use the SST from OAFflux. This choice is for consistency with the heat flux anomaly calculations (section 2.3). The numerical weather prediction reanalyses in OAFflux use the Reynolds et al. [2007] optimum interpolation AVHRR weekly SST product as a lower boundary condition. Therefore, OAFflux also uses Reynolds AVHRR SST because the consistency between air temperature and SST might worsen if OAFflux used AMSR-E SST [Yu et al., 2008]. The composite SST anomaly results below are qualitatively similar regardless of whether we use AMSR-E or OAFflux SST.

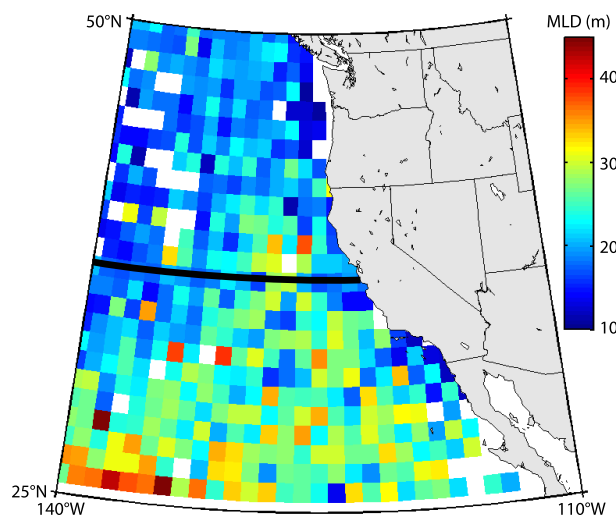


Figure 2. Mixed-layer depth climatology for the summer months of June–August from Argo floats (MLD depths from *Holte et al.* [2010]). The black line is 37°N and intersects the coast north of Monterey Bay, CA. The mean mixed-layer depth north (south) of the black line is 19.5 m (25 m).

gradients of density to determine a suite of possible MLDs [*Holte and Talley*, 2009]. The final MLD is chosen based on spatial patterns in the suite. In our study, we are interested in MLD as an indicator of the depth of mixing of water parcels, so we use the density algorithm MLD rather than the alternative temperature-based version.

The 10 day time interval between profiles from a single Argo float does not resolve the synoptic variations in the ~ 12 day wind event cycle, so we cannot use a time-varying MLD for the heat budget analysis. Instead, we use the mean MLD for June–August 2000–2015 at each grid point in the Argo data. The MLD values are highly variable in space, but smaller in the northern part of our study region than in the southern part (Figure 2). Therefore, for the northern wind relaxations we use the mean MLD poleward of 37°N: $h = 19.5$ m. For the southern relaxations, we use the mean MLD equatorward of 37°N: $h = 25$ m. The standard deviation of MLD calculated at each grid point and then averaged over the north (south) region is 5.5 (7.7) m.

2.6. Satellite Vector Wind Stress and Curl and Ekman Pumping

To estimate wind stress curl, instead of the OAF flux wind velocity, we use higher-resolution data from the SeaWinds microwave scatterometer on the Quick Scatterometer (QuikSCAT) satellite. Vector wind velocity data are available from QuikSCAT during 1999–2009. QuikSCAT obtained global swath measurements of wind velocity by transmitting microwave pulses and measuring the power backscattered from the ocean surface [e.g., *Tang et al.*, 2004]. We use the QuikSCAT Level 2B Version 3.0 swath data [*SeaPAC*, 2013; *Fore et al.*, 2014]. Following *Fewings et al.* [2016], we calculate the wind stress $\vec{\tau}$ from the QuikSCAT 10 m equivalent neutral wind velocity using the neutral stability drag coefficient determined by the COARE 3.5 bulk algorithm [*Edson et al.*, 2013]. We estimate the wind stress curl for each swath using the circulation theorem with five grid points, following previous studies [*Bourassa and McBeth Ford*, 2010; *Holbach and Bourassa*, 2014, 2017]. The wind stress and curl from each swath are then interpolated onto a 0.1° latitude-longitude grid.

We convert the wind stress curl into a vertical Ekman pumping velocity, w_{Ek} , which contributes to the vertical velocity at the base of the mixed layer, w_{-h} , and is proportional to wind stress curl [e.g., *Kraus and Businger*, 1994]:

$$w_{Ek} = \frac{\nabla \times \vec{\tau}}{\rho f} \quad (11)$$

where f is the Coriolis parameter.

2.5. Mixed-Layer Depth

We use existing mixed-layer depth estimates based on Argo float data. Argo floats are quasi-Lagrangian, vertically profiling instruments that sample the open ocean at a rate of approximately one profile every 10 days per $\sim 3^\circ$ latitude-longitude area (<http://www.argo.net>, <http://www.argo.ucsd.edu>). The floats descend to ~ 2000 m and drift for 10 days before returning to the surface, with descent and ascent speeds of $\sim 10 \text{ cm s}^{-1}$. Measurements occur on the ascent with a vertical resolution of ~ 10 m and stop ~ 5 m below the surface.

We use existing Argo float MLD estimates provided at <http://mixedlayer.ucsd.edu> [*Holte et al.*, 2010]. The MLD is calculated with a hybrid method that uses both density changes over the ML and vertical gra-

2.7. Constructing Composite Anomalies

We construct composite anomalies of SST, surface heat flux, and wind stress curl for each stage of the wind event cycle. The method is the same as in *Fewings et al.* [2016], except the method for removing a seasonal climatology differs depending on whether the data have gaps. We identify the wind relaxation start times using the *Melton et al.* [2009] index, which essentially requires the wind velocity near Point Conception, California, to be weaker than the mean for the following 2 days. Following multiple previous studies, we reject ~15% of the events because they are associated with landfalling fronts, which are not the focus of this study (see *Fewings et al.* [2016] for details). There are 44 remaining wind relaxations at Point Conception during the summer months of June–August 2002–2009.

We next remove a seasonal climatology at each grid point. The OAF flux and ISCCP products have no missing values, making filtering straightforward. Therefore, we calculate anomalies at each latitude–longitude location by removing the annual cycle using a high-pass filter with a 50 day half-amplitude cutoff. In contrast, the QuikSCAT wind stress and AMSR-E SST products have times of missing data. For wind stress and curl, we follow *Fewings et al.* [2016] and calculate anomalies by removing the summer mean over all years at each latitude–longitude grid point. For AMSR-E SST, to remove the seasonal climatology, we subtract the best fit linear trend, based on June–August 2002–2009, at each grid point.

We then construct composite average anomalies for each day from 10 days before to 10 days after wind relaxation at Point Conception, though only days -6 to $+6$ are shown here. For the QuikSCAT data, the morning and evening data are averaged separately and then the results averaged together to avoid bias toward one part of the diurnal cycle near the coast (see *Fewings et al.* [2016] for details). For the AMSR-E data, we only use nighttime data. In the composite anomaly figures below, gray shading indicates anomalies that are not significant at the 95% confidence level.

To answer our first question, regarding whether anomalies in the surface heat flux are the main driver of the SST anomalies during the 12 day event cycle, we map the daily evolution of the composite anomalies of ΔSST_{Obs} and $\Delta SST_{Q_{net}}$ from the 1-D mixed-layer heat budget (equation (2)) and then calculate ΔSST_{Res} as the difference. To answer the second question, regarding which surface heat flux components are the main contributors to the net surface heat flux, we map the daily evolution of the composite anomalies in net surface heat flux Q_{net} and its components: Q_{LHF} , Q_{SHF} , Q_{SWR} , and Q_{LWR} . We take a closer look at the anomalies in net LWR, Q_{LWR} , by calculating the anomalies of the downwelling and upwelling components, LWR_d and LWR_u . We then consider the composite anomalies in wind stress curl and whether the resulting Ekman pumping anomalies contribute substantially to observed changes in SST.

2.8. Separating the Northern and Southern Wind Relaxations

The SST and surface heat fluxes respond very differently during the northern and southern wind relaxations. We divide section 3 below accordingly. For the purpose of this study, we define the northern wind relaxation as the 6 days before the onset of wind relaxation at Point Conception (days -6 to -1), based on the wind stress anomaly composites in *Fewings et al.* [2016] (blue contours in top plots of Figure 3). We define the southern wind relaxation as beginning with the onset of wind relaxation at Point Conception and ending 5 days later (days 0 – 5 ; blue contours in bottom plots). As a result of splitting the analysis for the two relaxations, the reference time t_0 for calculating ΔSST_{Obs} and $\Delta SST_{Q_{net}}$ (equations (2)–(4)) is day -6 for the northern wind relaxation and day 0 for the southern wind relaxation. This allows for a clear picture of the changes in the SST over a 6 day period during each relaxation instead of combining the SST changes from the entire event cycle.

3. Results

3.1. Regional SST Anomalies During the Three-Stage Wind Event Cycle

There are two substantial SST anomalies during the wind event cycle, one warm and one cold (Figure 3). During days -6 to $+2$, there is a warm anomaly extending from ~250–1500 km offshore of northern and central California (red shading). The average anomaly is ~0.5°C. The magnitude of this warm anomaly is likely underrepresented in the composite average due to blurring of individual northern events with start times that vary relative to the onset of the southern wind relaxation, which is the basis for the compositing. The warm SST anomaly has largest spatial extent on days -2 to $+1$. This timing differs from the timing of

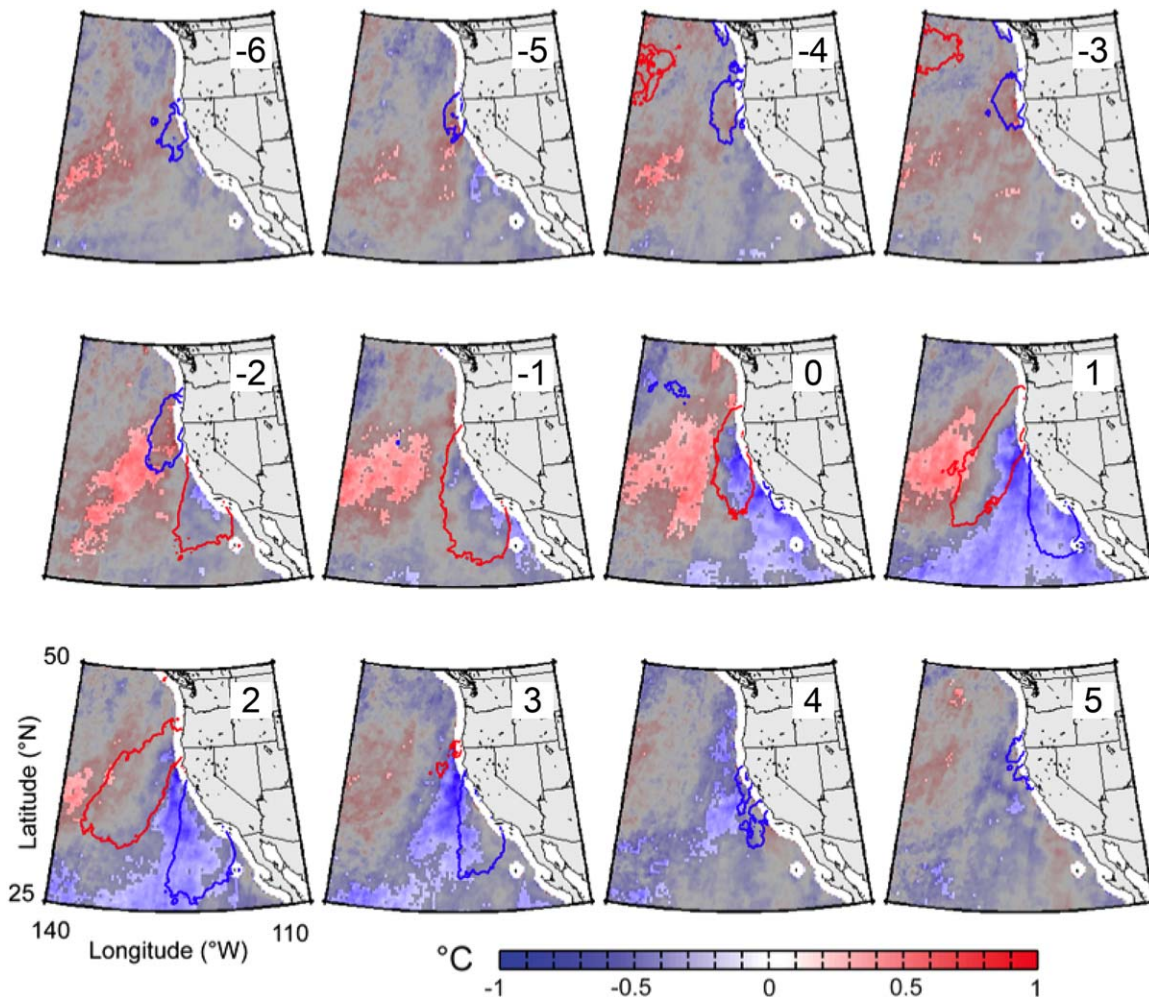


Figure 3. Time evolution of SST and wind stress anomalies during the 12 day event cycle. The number in upper right of each plot indicates time in days, relative to the onset of wind relaxation at Point Conception (day 0). Color shading shows composite satellite SST anomalies from AMSR-E, based on 44 wind relaxations at Point Conception during June–August 2002–2009. Blue (red) indicates colder (warmer) than the climatological SST at that location. Grey shading indicates that the anomaly is not significant at the 95% confidence level. Contours of along-mean wind stress anomaly = ± 0.03 Pa from QuikSCAT data are overlaid in red and blue, respectively [from *Fewings et al.*, 2016, Figure 6] (the along-mean direction is defined as the direction of the mean wind stress in Figure 1 above).

the northern wind relaxation, which has largest extent on days -4 to -2 (blue contours in upper row) and is weakening by the time the warm SST anomaly reaches its maximum extent. The warm anomaly persists during the time of the wind intensification (red contours) that follows the northern wind relaxation, though the warm anomaly is restricted to outside the area where the wind is intensified (red shading and red contour, days 0–2). Therefore, relative to the time of the northern wind relaxation, the warm SST anomaly develops with a lag of a couple of days.

During the wind reintensification (red contours in Figure 3), an SST anomaly develops that is stronger and negative, $\sim -1^{\circ}\text{C}$. This cold anomaly (blue shading) eventually extends ~ 2000 km along the coast from northern California along Baja California and ~ 2000 km offshore to the southwest. The cold anomaly begins near the coast during the time the upwelling-favorable winds reintensify and in the same location along the coast (red contours and blue shading, days -2 to 2). Again, the development of the SST anomaly appears to lag the wind reintensification by a couple of days, similarly to the wind-SST lag during the northern wind relaxation above. The cold anomaly persists throughout the time of the southern wind relaxation. During the beginning of the southern wind relaxation, the weak wind stress and negative SST anomalies are colocated (blue contours and shading, days 0–2). There is a marked contrast in the relationship between the wind stress and SST anomalies during the northern versus southern wind relaxations. During the northern wind relaxation, the SST anomaly is located offshore of the strongest wind stress anomaly and has the

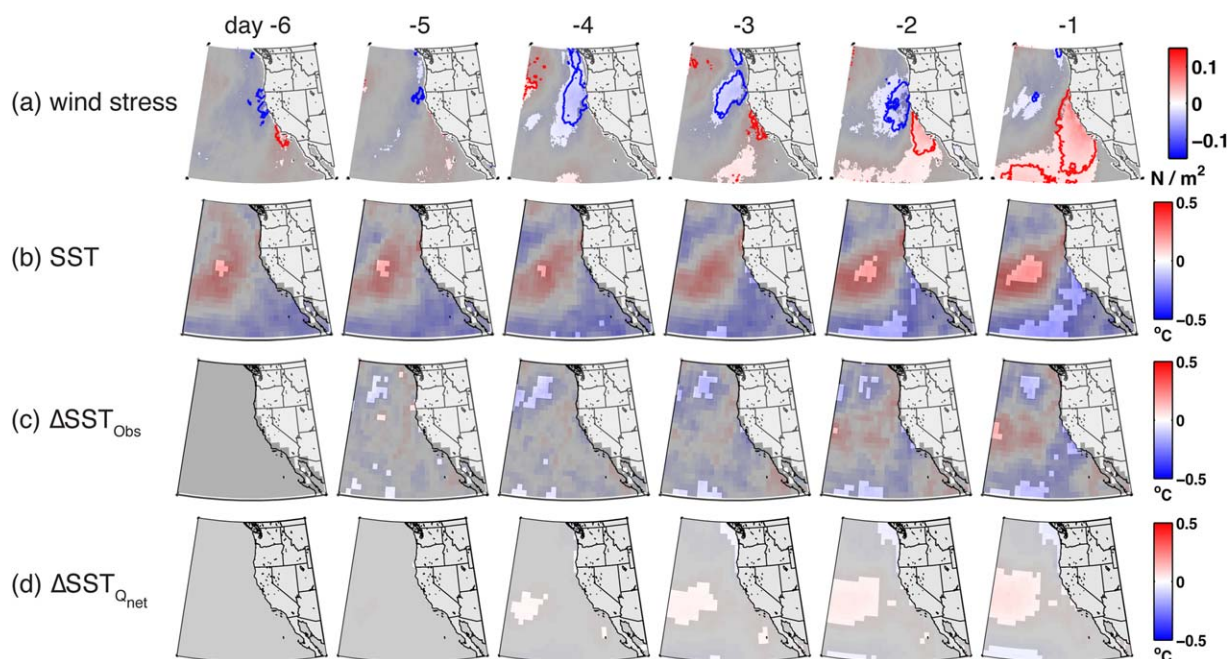


Figure 4. Time evolution of composite anomalies in wind stress and SST during the northern wind relaxation. The composited anomalies are (a) along-mean wind stress from QuikSCAT, as in *Fewings et al.* [2016]; (b) SST from OAFlux based on 44 events from June–August 2002–2009; (c) the change in SST since the start of the relaxation, ΔSST_{Obs} ; and (d) the change in SST since the start of the relaxation predicted from surface heat flux alone, $\Delta SST_{Q_{net}}$. The number in each plot indicates time in days relative to the onset of wind relaxation at Point Conception buoys (day 0, not shown in figure). Color indicates the anomaly: blue indicates weaker wind stress or colder SST. Latitude and longitude range is the same as in previous figures.

opposite sign. During the southern wind relaxation, the SST anomaly extends to the coast and has the same sign as the wind stress anomaly. Composite SST anomalies based on OAFlux SST show similar patterns (e.g., Figure 4b). To understand this contrast between the SST responses to northern and southern wind relaxations, we consider the time-integrated heat budget.

3.2. Heat Budget for the Northern Wind Relaxation

3.2.1. Testing a 1-D Heat Budget for the Mixed Layer

To determine whether the main driver of the SST anomalies during the northern wind relaxations is the surface heat flux Q_{net} , we examine the evolution of the terms in the 1-D ML heat budget (equation (6)). Over the 6 days of the northern relaxation, the observed change in SST and the predicted change based on surface heat flux alone both accumulate positive anomalies in the offshore region where the positive SST anomaly is strongest (Figures 4c and 4d). The residual in the region of this warm SST anomaly is small, $\sim 10\%$ of ΔSST_{Obs} (Figure 5). Therefore, the surface heat flux anomaly explains $\sim 90\%$ of the warm SST anomaly as a whole. However, the residual is larger in the region where the warm SST anomaly is strongest; there, the surface heat flux explains only $\sim 45\%$ of the SST anomaly (small red area at left in Figure 5c). We conclude that vertical mixing and advection and other terms that contribute to the residual in the 1-D heat budget (equation (5)) are not necessary to explain the majority of the warm SST anomaly that occurs offshore during the northern wind relaxations, but these terms are needed to explain the strongest part of the SST anomaly.

3.2.2. Atmosphere–Ocean Heat Flux Anomalies: Northern Relaxation

To determine which surface heat flux components are the main contributors to the net surface heat flux anomalies during the northern wind relaxations, we examine composite anomalies of Q_{net} , SWR, LWR, LHF, and SHF over the 44 wind events (Figure 6). Plots of the monthly means of these variables are available in *Flynn* [2016]. The surface heat flux Q_{net} from day -6 to day -1 shows three anomalies. The first is a slight negative anomaly (reduced ocean warming, Figure 6a, blue) off the Pacific Northwest. This is the result of a decrease in shortwave radiation associated with northern wind relaxations (Figure 6b, blue in days -6 to -3), which is typically due to increased cloudiness [e.g., *Iacobellis and Cayan*, 2013]. The second Q_{net} anomaly appears off the coast of Baja California at day -1 (Figure 6a, blue in right plot), also associated with reduced shortwave radiation (Figure 6b, blue in right plot). This anomaly is associated with the onset of the

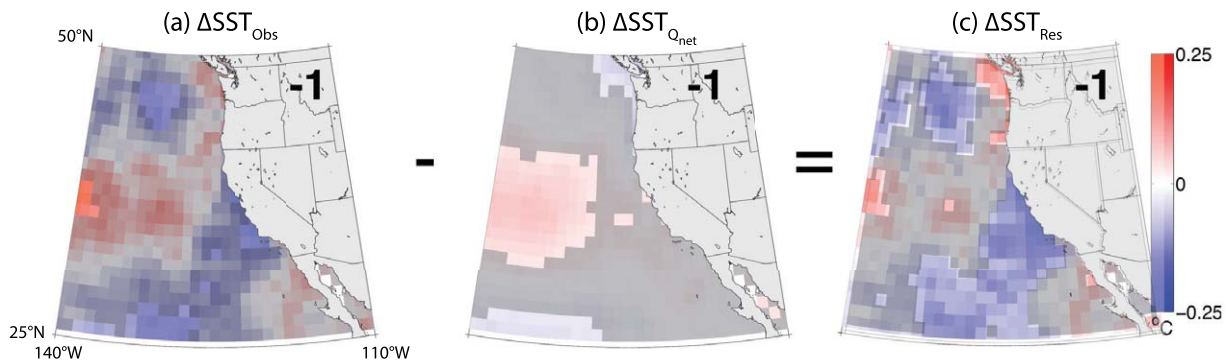


Figure 5. Time-integrated 1-D heat balance during the northern wind relaxation. (a–c) The three terms in equation (6), respectively, calculated from the composite anomalies of SST and Q_{net} based on equations (3)–(5) with $t_0 = -6$ and $t = -1$. (a) Composite anomaly of $SST(\text{day} - 1)$ minus $SST(\text{day} - 6)$. (b) Composite anomaly of the predicted change in SST from surface heat flux alone. (c) Composite anomaly of the residual, calculated by subtracting the anomalies in Figure 5b from Figure 5a. In Figure 5a, blue (red) indicates a smaller (larger) SST change over the 5 day period of the northern wind relaxation than in the climatology. In Figures 5b and 5c, blue (red) indicates anomalous surface water cooling (heating). Grey indicates the anomaly is not significantly different from zero at the 95% confidence level.

southern wind relaxations and is discussed in section 3.3.2 below. The third Q_{net} anomaly is the prominent positive anomaly (ocean warming) that appears from days -5 to -1 (Figure 6a, red), dominating the cumulative surface heat flux anomaly discussed in section 3.2.1 (red in Figure 4d). This positive Q_{net} anomaly associated with the northern wind relaxation is a result of an increase in SWR (Figure 6b, red), a decrease in latent cooling (Figure 6d, red), and a small increase in the sensible heat flux (Figure 6e, red). Therefore, the offshore warming during the northern wind relaxation is caused mostly by reduced latent cooling (days -6 to -1 , most apparent on days -4 to -1) and increased shortwave radiation (days -2 and -1).

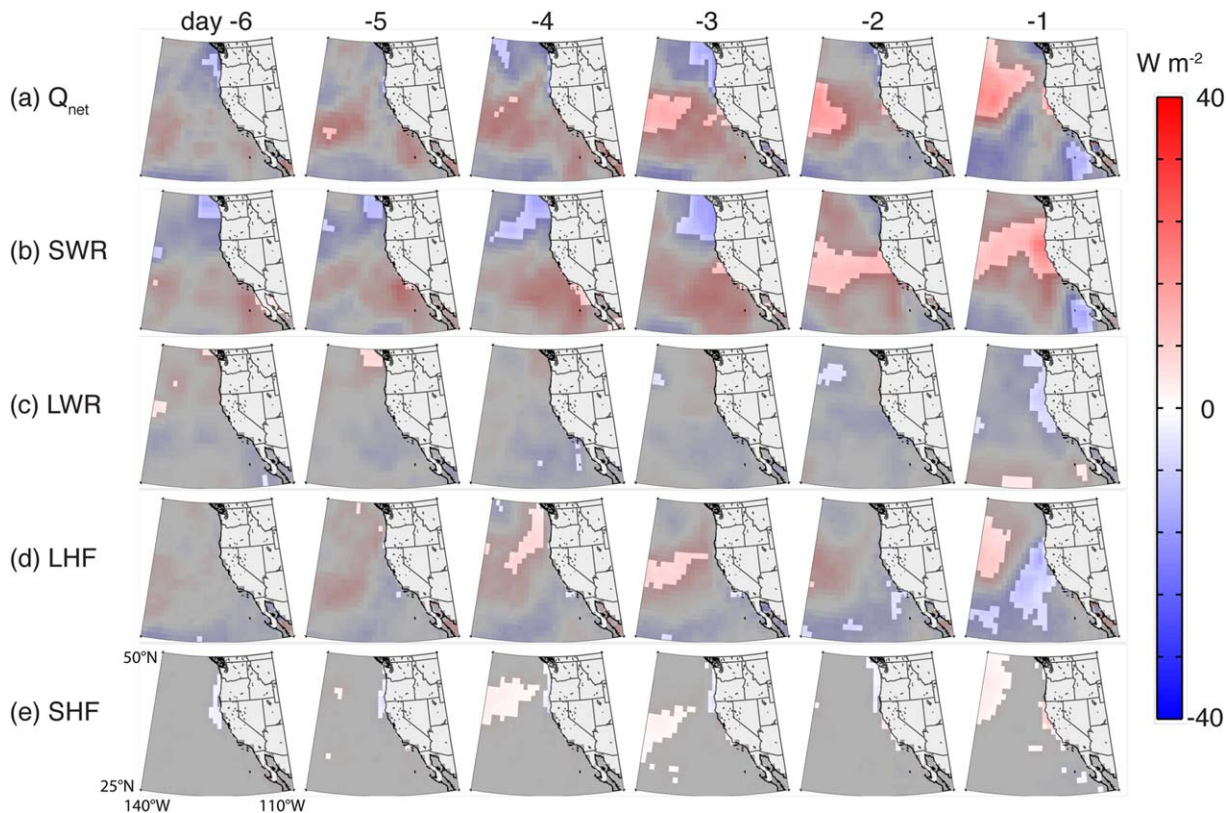


Figure 6. Time evolution of composite anomalies in the surface heat flux based on 44 northern wind relaxations from June–August 2002–2009. Positive (red) indicates more downward heat flux into the ocean than in climatology. The number above each column indicates time in days relative to the onset of wind relaxation at Point Conception buoys (day 0, not shown in figure). Color indicates the anomaly. The 50 day low-pass-filtered daily mean was removed from each grid point. Blue (red) indicates anomalous surface water cooling (heating). Grey indicates the anomaly is not significant at the 95% confidence level.

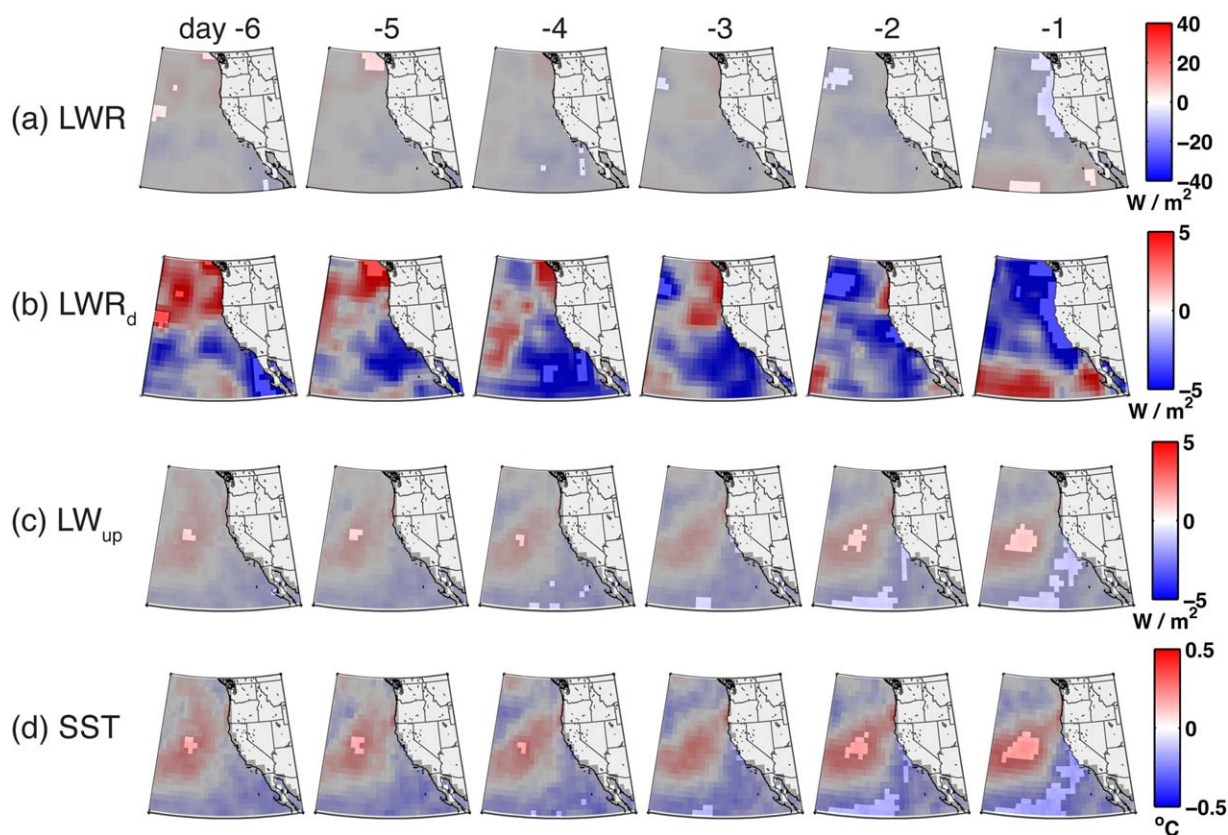


Figure 7. Time evolution of composite anomalies in longwave radiation based on 44 northern wind relaxations from June–August 2002–2009. The number in each plot indicates time in days relative to the arrival of the southern wind relaxation (day 0, not shown in figure). Grey indicates the anomaly is not significant at the 95% confidence level.

The anomalies in longwave radiation, though smaller than the LHF and SWR anomalies, are not negligible, particularly near the coast where the LWR anomaly is negative (Figure 6c). Unlike SWR, the downwelling and upwelling LWR components are affected by different processes (section 2.3) and should be examined separately. During the northern relaxations, LWR_d anomalies have a larger magnitude than LWR_u anomalies (Figures 7b and 7c). Therefore, the net negative LWR anomaly near the coast on day -1 (Figure 6c) is driven by a reduction in the incoming longwave radiation. Reductions in LWR_d are typically due to decreased cloudiness [e.g., *Iacobellis and Cayan, 2013*], which is consistent with the positive shortwave radiation anomaly in the same region (Figure 6b). In contrast to LWR_d , the upwelling longwave radiation is mainly dependent on SST (equation (9)), and thus anomalies in LWR_u mimic the SST anomalies (Figures 7c and 7d).

3.3. Heat Budget for the Southern Wind Relaxation

3.3.1. Testing a 1-D Heat Budget for the Mixed Layer

For the southern wind relaxation, we again use a 1-D ML heat budget to determine whether the main driver of the SST anomalies is the net surface heat flux. In the case of the southern wind relaxation, there are strong preexisting SST anomalies (Figure 8b, day 0), including a cold SST anomaly in the area where the wind relaxation develops, along the coast of central California and extending offshore to the southwest (blue in Figure 8a). However, there is a positive trend in SST in that offshore area after the onset of wind relaxation (red in lower part of Figure 8c). Over 6 days, both the observed change in SST and the change predicted from surface heat flux alone are positive in the southern part of the study area, offshore, though the change in SST predicted from surface heat flux anomaly $\Delta SST_{Q_{net}}$ is smaller than the observed change (red in lower parts of Figures 8c and 8d). However, near the coast of central and southern California the surface heat flux anomaly is zero or negative (small blue area in Figure 8d, day 5), the wrong sign to explain the observed temperature trend.

In contrast to the northern wind relaxation, then, surface heat flux explains only part (<25%) of the observed warming trend in SST offshore during the southern relaxation and cannot explain the warming in

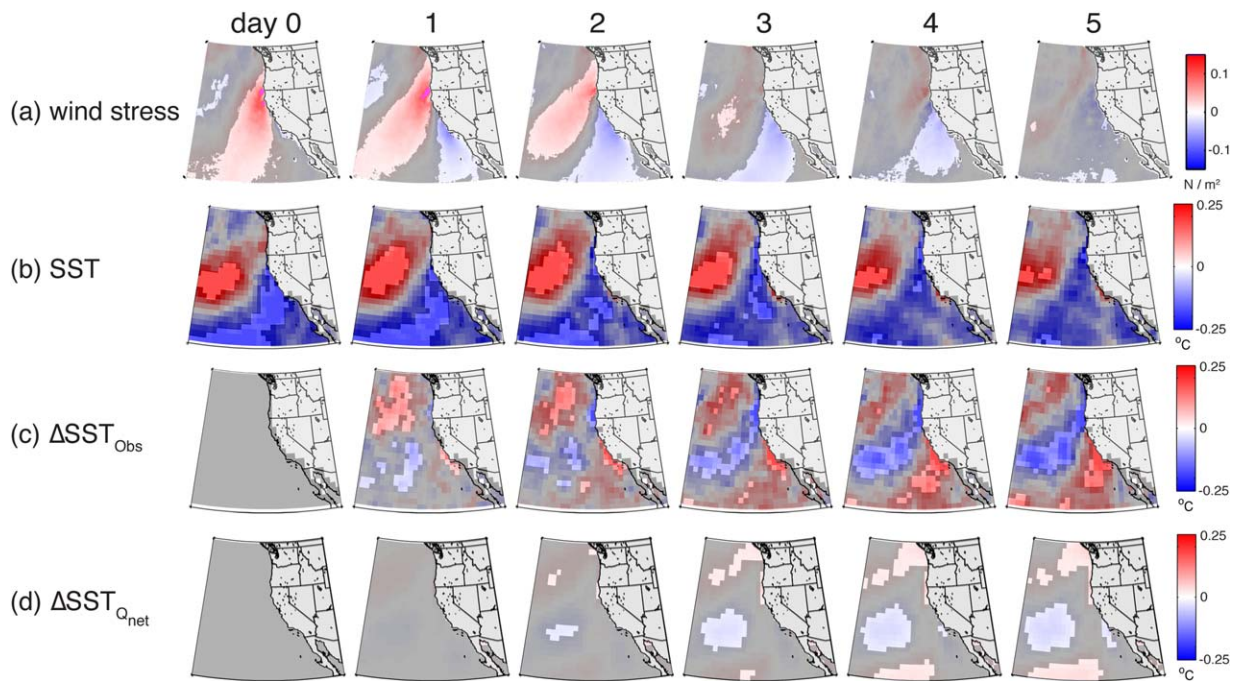


Figure 8. Time evolution of composite anomalies in wind stress and SST, similar to Figure 4 but for the southern wind relaxation. The number in each plot indicates time in days relative to the onset of wind relaxation at Point Conception buoys (day 0). Note that the color scale in Figures 8b and 8c differs from Figure 4.

SST near the coast (Figure 9). The residual in the 1-D heat budget is large. We must examine individual terms in the residual, ΔSST_{Res} , in equation (6) to determine what drives the SST anomalies during the southern wind relaxations. This is addressed in section 4 below.

3.3.2. Atmosphere-Ocean Heat Flux Anomalies: Southern Relaxation

Above, we showed that there are not large anomalies in net surface heat flux in the area of the southern wind relaxation, unlike during the northern relaxation. To determine why, we examine the magnitude and evolution over time of each component of the net surface heat flux anomaly.

The surface heat flux Q_{net} from days 0 to 5 shows three anomalies, but only one is associated with the southern wind relaxations. The first is a positive heat flux anomaly offshore of the Pacific Northwest from days 0 to 2 (Figure 10a, red in upper part of plots). This anomaly is mainly a result of an increase in SWR (Figure 10b, red) and a decrease in latent cooling (Figure 10d, red). This anomaly is associated with the end of the northern wind relaxation and was discussed in section 3.2.2. The second is a negative anomaly offshore of California and Baja California (Figure 10a, blue), due to stronger latent cooling associated with the wind reintensification that occurs between the northern and southern relaxations (Figure 8a, red and Figure 10d,

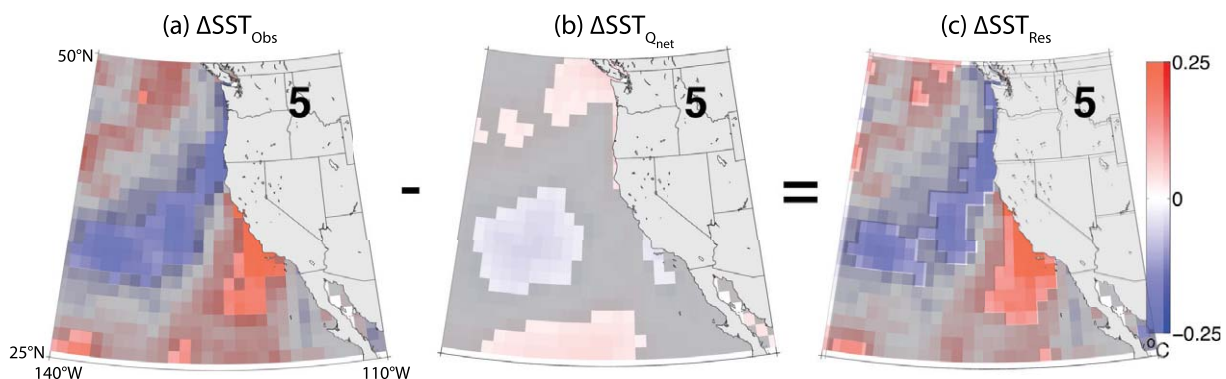


Figure 9. Time-integrated 1-D heat balance, similar to Figure 5 but for the southern wind relaxation, with $t_0 = 0$ and $t = 5$.

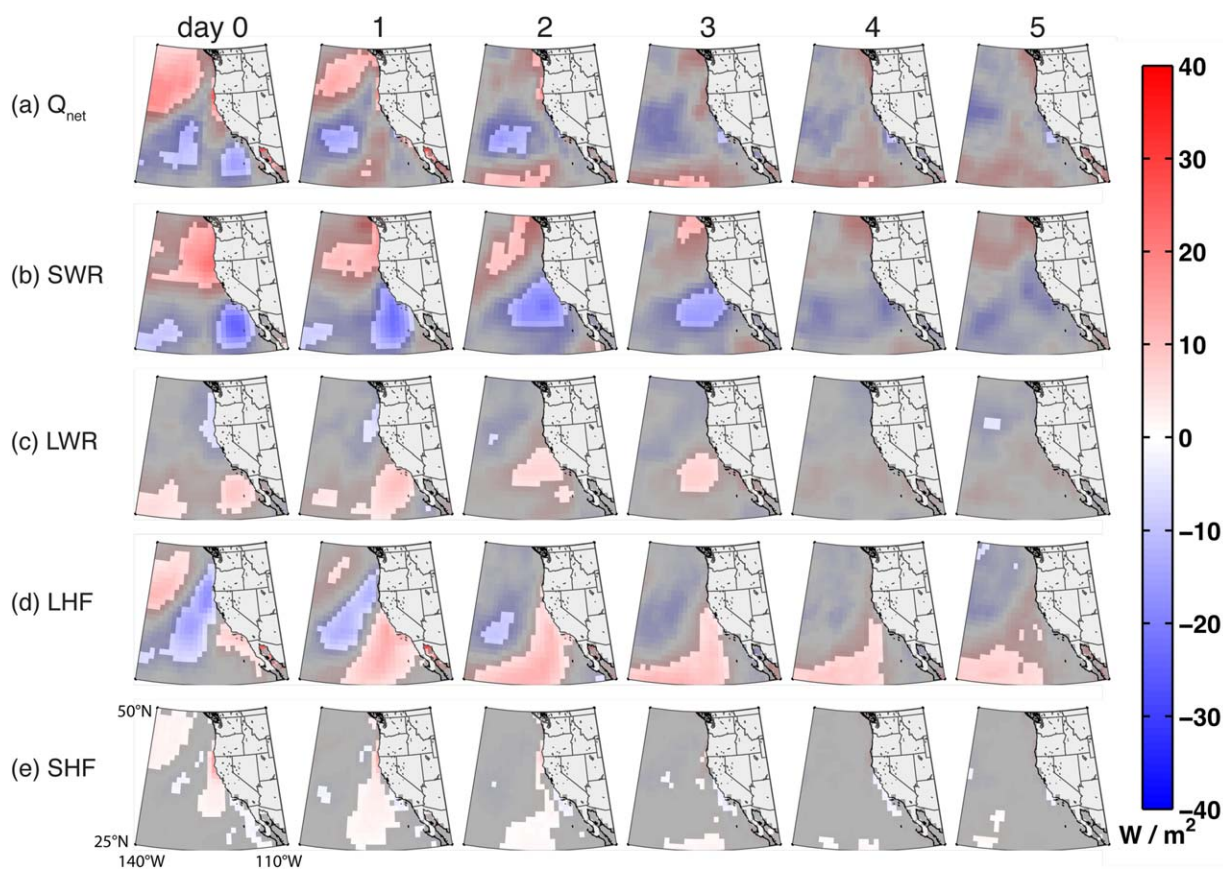


Figure 10. Time evolution of composite anomalies of the surface heat flux, similar to Figure 6 but for the southern wind relaxations.

blue). There is also a contribution near the coast from reduced SWR, presumably due to increased clouds, which are commonly associated with the onset of southern wind relaxations and the rarer reversals [e.g., Nuss *et al.*, 2000] (Figure 10b, blue, day 0).

The third surface heat flux anomaly is associated with the southern wind relaxations. It is a weak positive anomaly (ocean warming) offshore to the west of Baja California from days 1 to 3 (Figure 10a, red in central lower part of plots). This anomaly is a result of a decrease in latent cooling (Figure 10d, red) from the decrease in wind forcing during the southern wind relaxations (Figure 8a, blue). This positive surface heat flux anomaly is consistent with the sign of the anomaly expected during a wind relaxation. However, a question remains: why, in contrast to the northern wind relaxation, is there no positive surface heat flux anomaly near the coast of central California where the main part of the southern wind relaxation is located, and instead an area of near zero or negative surface heat flux anomaly (Figure 10a, days 1–3)?

The small net surface heat flux anomaly along the coast of central California during the southern wind relaxation is a consequence of opposing latent and shortwave heat flux anomalies. The latent heat flux anomaly is positive along central and southern California, as expected for weaker winds and reduced latent cooling (Figure 10d). However, there is also a strong decrease in the incoming solar radiation (Figure 10b, blue). This is presumably due to cloudiness [Jacobellis and Cayan, 2013], consistent with the positive LWR anomalies (Figure 10c, red) observed in the same spatial region. It is typical for the net effect of low, thick marine stratus clouds to be a cooling effect, because the clouds reduce the incoming shortwave radiation more than they increase the downwelling longwave radiation [Hartmann *et al.*, 1992; Klein and Hartmann, 1993]. As a result, the net surface heat flux anomaly along the central California coast is near zero during days 1–3 of the southern wind relaxation (Figure 10a).

The downwelling LWR anomalies during the southern wind relaxations (Figure 11b) are larger in amplitude than those in the northern wind relaxations (Figure 7b), whereas the upwelling LWR anomalies are similar

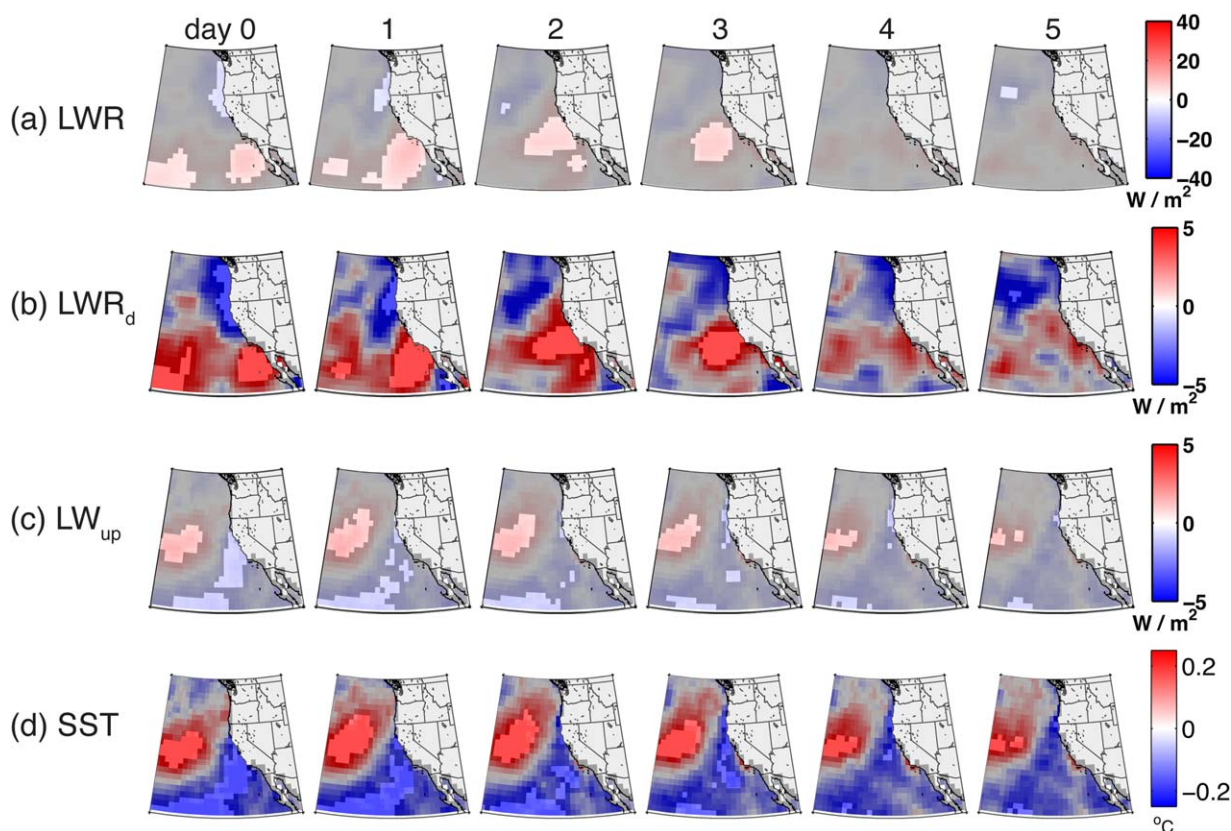


Figure 11. Time evolution of composite anomalies of longwave radiation, similar to Figure 7 but for the southern wind relaxations.

(Figures 7c and 11c). This makes sense because there is a greater increase in cloudiness, presumably the previously described low marine stratus [e.g., *Iacobellis and Cayan, 2013*], during the southern wind relaxations, but an SST anomaly of similar magnitude. The result is that the net LWR anomaly is positive and larger during the southern than northern wind relaxations (Figures 7a and 11a). However, the positive LWR anomaly is not strong enough to overcome the negative SWR anomaly discussed above (Figure 10b). The main effect during the southern wind relaxations is that the SWR anomaly opposes the latent heat flux anomaly, leading to near-zero net surface heat flux anomaly near the coast.

4. Discussion

4.1. Contrasting Causes of SST Anomalies During the Northern and Southern Wind Relaxations

During the northern wind relaxation, the warm SST anomalies result mostly ($\sim 90\%$) from changes in the net surface heat flux components, especially the latent heat flux, with some contribution from shortwave radiation. Thus, we do not need the residual to qualitatively explain the SST anomaly, and the 1-D heat budget (equation (2)) is appropriate. Where the warm SST anomaly is largest, however, the left side of equation (2) accounts for less of the anomaly ($\sim 45\%$). In that smaller region, the other terms in the 3-D heat budget (equation (1)) must be more important, similarly to what is discussed below for the southern wind relaxation.

At the onset of the southern wind relaxation, there is a preexisting cold SST anomaly caused by the wind reintensification that occurs beforehand. During the subsequent relaxation, there is a warming trend in SST, similar to the northern wind relaxation. However, in contrast to the northern relaxation, the 1-D heat budget (section 3.3.1) indicates the driver of this warming trend is not the net surface heat flux. This is because there is a stronger reduction in shortwave radiation during the southern wind relaxations than the northern, which offsets the reduced latent cooling, leading to a near-zero anomaly in net surface heat flux. This leads to the question: What terms in the time-integrated 1-D heat budget residual are driving the SST anomalies

during the southern relaxations? Below, we estimate the remaining terms in equation (2): penetrating solar radiation, horizontal advection, and horizontal diffusion, and discuss implications for entrainment and Ekman pumping.

4.2. Penetrating Solar Radiation

In the surface heat flux analyses based on OAFlux, we did not correct for the penetrating radiation because we do not know the optical attenuation coefficient and ML depth as a function of time. However, we can estimate the amount of radiation that penetrates past the base of the mixed layer following *Paulson and Simpson* [1977]:

$$SWR_{-h} = SWR_0 \left(R \cdot e^{-\frac{h}{\zeta_1}} + (1-R)e^{-\frac{h}{\zeta_2}} \right) \quad (12)$$

where SWR_{-h} is the radiative flux at the base of the ML, $z = -h$; SWR_0 is the shortwave radiative flux at the sea surface; $R = 0.62$; and the attenuation lengths are $\zeta_1 = 1.5$ m and $\zeta_2 = 20$ m. The first term on the right-hand side accounts for the far infrared spectral components that are mostly absorbed within the first few meters of the ML, and the second term represents the shortwave (ultraviolet, visible, and near infrared) spectral components. For the southern wind relaxation, we use a MLD of 25 m (section 2.5). Then $SWR_{-h} = 0.11 SWR_0$, so the penetrating radiative flux through the base of the ML is $\sim 10\%$ of the composited SWR computed from OAFlux.

The contribution of the penetrating radiation to the residual in the 1-D heat budget, based on equation (2), is then

$$\Delta SST_{Res B} = \int_{t_0}^t -\frac{SWR_{-h}}{\rho_w c_p h} dt = -0.11 \int_{t_0}^t \frac{SWR_0}{\rho_w c_p h} dt \quad (13)$$

Because the anomaly in SWR_0 is negative in the area of the southern wind relaxation (blue in Figure 10b), the contribution of penetrating radiation to the residual (equation (13)) for the SST anomaly budget will be positive. This is the same sign as the observed residual (red in Figure 9c), suggesting the penetrating radiation might explain the residual. However, the magnitude of the penetrating radiation anomaly is only $\sim 10\%$ of the SWR anomaly (equation (13)). The SWR anomaly is comparable to the net surface heat flux anomaly (compare amplitudes in Figures 10a and 10b), which is small compared to the observed total residual in the anomaly budget (Figures 9b and 9c); 10% of this value will be negligible. Therefore, even though the neglected solar penetrating radiation term has the needed sign, we conclude that it cannot explain the residual in the heat budget.

4.3. Horizontal Advection of SST Gradients

We estimate the time-integrated horizontal advection of SST gradients using equation (2), term C:

$$\Delta SST_{Res C} = \int_{t_0}^t -\bar{u} \cdot \nabla_H SST dt = O \left(U \frac{\Delta T}{\Delta X} \Delta t \right) \quad (14)$$

where U is the scale of the horizontal current, $\Delta T/\Delta X$ is the scale of the horizontal SST gradient, and $\Delta t = t - t_0$. The mean horizontal current speed away from land in the southern end of the CCS is $O(0.1 \text{ m s}^{-1})$ [Brink *et al.*, 1991]. The mean SST in the region of the southern wind relaxation changes by $O(1^\circ\text{C})$ over a distance of ~ 100 km (e.g., Figure 1). With $t - t_0 = 6$ days, equation (14) indicates the contribution of horizontal advection of SST gradients to ΔSST_{Res} is $O(0.5^\circ\text{C})$. It is reasonable to use the size of the mean term (equation (14)) as an estimate of the maximum possible size of the anomaly because the wind stress forcing anomalies during the southern relaxations are the same size as the mean [Melton *et al.*, 2009; Fewings *et al.*, 2016]. Therefore, the estimated change in SST due to horizontal advection of SST gradients is the same order as the total residual in the SST anomaly budget (Figure 9). The expected sign of this term off southern California is also consistent with the residual. During wind relaxation, there is a reduction or reversal in the southward advection of cold water past Point Conception, CA [Harms and Winant, 1998; Winant *et al.*, 2003]; in addition, during wind relaxations, there is increased northward advection of warmer water associated with the Southern California Bight recirculation gyre and the poleward countercurrent [Hickey, 1979; Lynn and Simpson, 1987; Washburn *et al.*, 2011]. Therefore, though we do not have horizontal water velocities to estimate this term during each of the 44 wind relaxations, it is plausible that

advection of horizontal SST gradients explains part of the residual in the heat budget near the coast during the southern wind relaxation.

4.4. Horizontal Eddy Diffusion of Heat

We estimate the time-integrated horizontal heat diffusion using equation (2), term D:

$$\Delta SST_{Res,D} = \int_{t_0}^t \kappa_H \nabla_H^2 SST \, dt = O\left(\kappa_H \frac{\Delta T}{(\Delta X)^2} \Delta t\right) \quad (15)$$

In the southern end of the CCS, the horizontal eddy diffusivity is $O(10^3 \text{ m}^2 \text{ s}^{-1})$ [Swenson and Niiler, 1996]. As in section 4.3, the SST changes by $O(1^\circ\text{C})$ over a distance of ~ 100 km. Therefore, over 6 days, $\Delta SST_{Res,D} \sim 0.05^\circ\text{C}$. Again assuming the anomaly in this term would be the same order as the mean, the contribution of horizontal eddy diffusion of heat to the observed SST anomalies is negligible. This is consistent with prior work suggesting that eddy diffusion of heat is not important in the upper ocean heat balance in the California Current system [Swenson and Niiler, 1996].

4.5. Vertical Entrainment and Ekman Pumping

We cannot directly estimate the contribution of entrainment to the time-integrated residual. If we used the sum of the terms in equation (2), term E, the uncertainty in the estimates would be too large, given that we have no observations of temporal or spatial changes in MLD ($\partial h/\partial t$ or $\nabla_H h$) on synoptic time scales (i.e., less than the 10 day resolution of the Argo float data). However, entrainment is expected to decrease with decreased wind stress, such as during a wind relaxation: decreased wind stress results in decreased wind-driven vertical shear and the resulting shear-driven mixing and entrainment at the base of the mixed layer [e.g., Stevenson and Niiler, 1983; Price et al., 1986]. Therefore, it is plausible that decreased entrainment of cold water due to the reduced wind stress contributes to the warming of SST with time during the southern wind relaxation, explaining part of the residual in the heat budget (section 3.3.1).

Ekman pumping (upwelling due to wind stress curl) can affect SST directly in regions where the isotherms are outcropping at the surface, such as in the upwelling region within ~ 200 km of the coast in the CCS (Figure 1). On average, during summer, there is a band of positive wind stress curl along the coast in the CCS [Bakun and Nelson, 1991], modified by a dipole of curl south of each of the major coastal capes [Perlin et al.,

2004; Chelton et al., 2007] (Figure 12). However, during the southern wind relaxation, there is a negative (downwelling-favorable) wind stress curl anomaly along the coast of central and southern California (Figure 13, days 1–5). The curl anomaly is equivalent to a reduction in vertical Ekman pumping velocity of $\sim 1 \text{ m d}^{-1}$. Given typical temperature stratification of $\sim 0.1^\circ\text{C m}^{-1}$ in the upper 20–30 m in the region of Point Conception [Palacios et al., 2004], this reduction in Ekman pumping would result in an SST warming over 6 days of $\sim 0.6^\circ\text{C}$, similar to the observed residual. Therefore, reduced Ekman pumping during wind relaxation should be important in creating the warming SST in the coastal upwelling region where the isopycnals typically outcrop. This is more important than solar warming of the surface waters, due to the increased cloudiness during relaxation.

4.6. Wind Stress—SST Feedbacks and Clouds

In addition to wind stress affecting SST, an SST anomaly can affect the overlying wind stress, as reviewed by Small et al. [2008]. Over the open ocean and in much of the CCS, on scales of

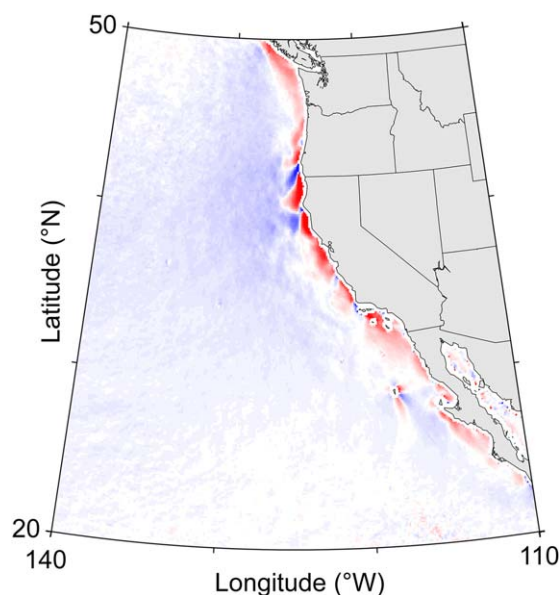


Figure 12. Mean wind stress curl during June–August 2002–2009 from QuikSCAT satellite ocean vector wind data. The blue-to-red color scale ranges from -2×10^{-6} to $+2 \times 10^{-6} \text{ Pa m}^{-1}$. Red indicates positive curl (implying divergent surface ocean currents, an upward Ekman pumping velocity, and oceanic upwelling) and blue indicates negative curl (downwelling). White indicates zero.

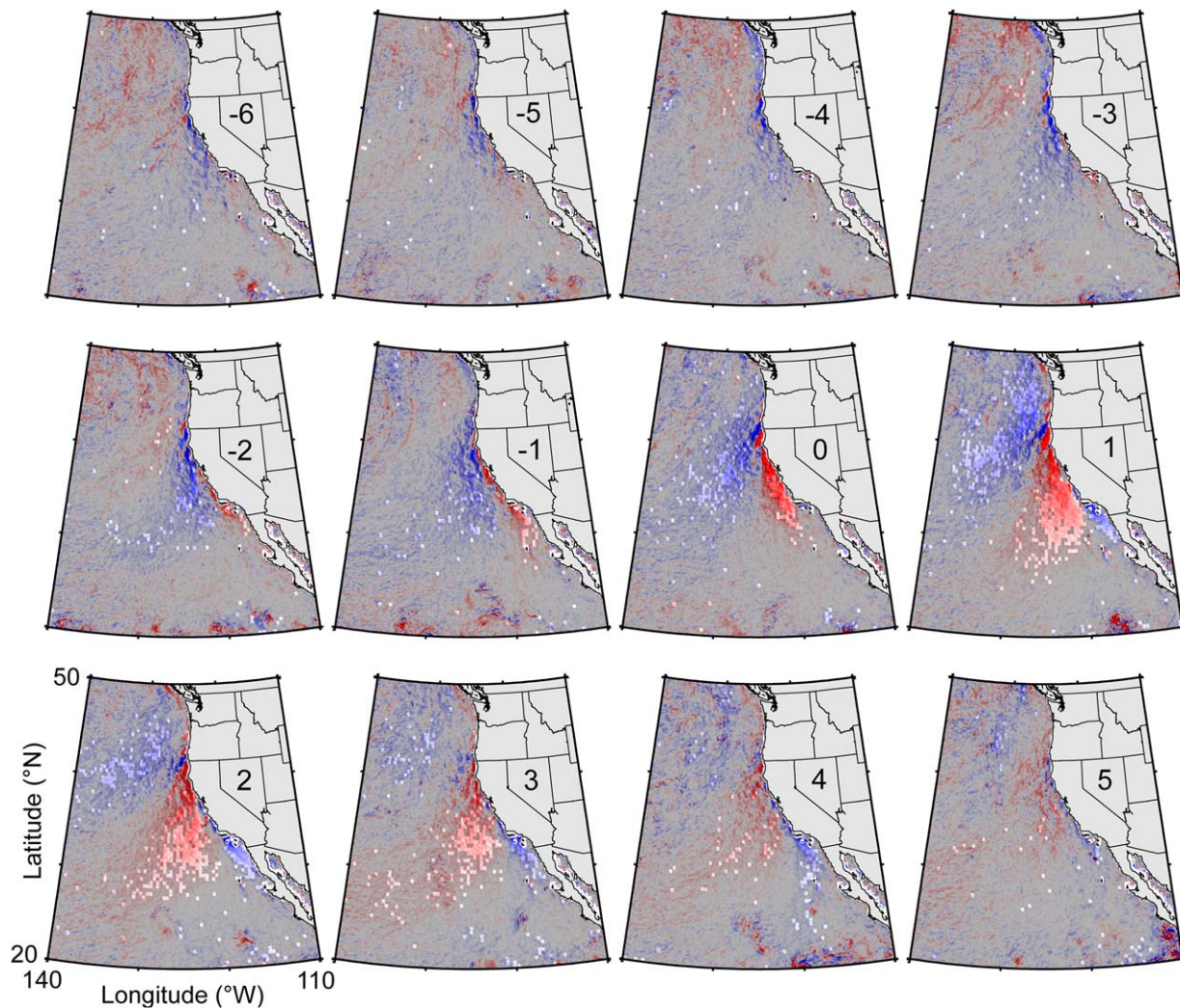


Figure 13. Time evolution of wind stress curl anomalies during the ~ 12 day wind event cycle, relative to the mean in Figure 12. The composite anomalies are calculated from wind stress curl from QuikSCAT satellite data for the 44 relaxations during June–August 2002–2009. The blue-to-red color scale ranges from -1×10^{-6} to $+1 \times 10^{-6}$ Pa m^{-1} . Red indicates positive curl anomaly and blue indicates negative curl anomaly. White indicates zero and grey indicates not significant. The number in upper right of each plot indicates days since the onset of the southern wind relaxation (day 0).

hundreds of kilometers there is a tendency for stronger surface stress over warmer water due to destabilization of the atmospheric boundary layer [Chelton *et al.*, 2007; Small *et al.*, 2008]. If this is the only process affecting the wind stress, the SST and wind stress anomalies will therefore tend to have the same sign, indicating the ocean is forcing the atmosphere. The surface heat flux anomaly will tend to be opposite in sign to the wind stress and SST anomalies, in the sign convention used here [Small *et al.*, 2008].

During the southern wind relaxations, there is in fact reduced wind stress over colder water (Figure 3). There are also accompanying positive latent and sensible heat flux anomalies (Figures 10d and 10e). Note that for the effect of SST on the atmospheric boundary layer and wind stress–SST feedback, we are concerned with the turbulent surface heat flux, not the radiative components. Therefore, it is not relevant for the feedback of SST onto wind stress that the net surface heat flux anomaly is near zero due to cancellation of the latent heat flux anomaly by the shortwave radiation anomaly (section 3.3.2). For example, the sensible heat flux anomaly during southern relaxations indicates anomalous warming of the ocean, implying anomalous cooling of the atmosphere, i.e., less than climatological warming (Figure 10e). This heat flux anomaly should increase the atmospheric boundary layer stability, potentially helping maintain the weakened wind stress during the southern relaxations. The heat flux anomaly could also, by cooling the atmospheric boundary layer, increase the strength of the temperature inversion at the top of the marine boundary layer and promote cloud formation (though many other factors affect inversion strength and cloud and fog formation as

well, such as changes in the temperature above the boundary layer, wind shear at the inversion height, or cloud top radiative cooling [see, e.g., Wood, 2012; Koračin *et al.*, 2005]. In the CCS region, increased inversion strength is associated with greater cloud cover and fog [Iacobellis and Cayan, 2013]. Increased cloudiness would contribute to reduced shortwave radiation, again leading to colder SST. Therefore, we infer that wind stress-SST-surface heat flux feedback, and possibly SST-cloud feedback, may act to prolong the southern wind relaxations.

However, during the northern relaxations and during the subsequent wind intensifications, the wind stress and SST anomalies have opposite signs and there is less spatial overlap of the anomalies (Figure 3). (Note that the wind stress anomaly does extend farther offshore, overlapping more with the SST anomaly, than the 0.03 Pa along-coast wind stress anomaly contour displayed here [see Fewings *et al.*, 2016, Figures 6 and 9].) The sign of the latent and sensible heat flux anomalies is what we would expect based on the observed wind stress anomaly, not the observed SST anomaly, indicating that the atmospheric forcing of the ocean is dominating during the northern relaxations, not the SST-wind stress feedback mechanisms reviewed in Small *et al.* [2008]. The effect of the SST anomalies during the northern wind relaxations and the wind intensifications would be to weaken, not create, wind stress anomalies of the observed sign.

Wind stress-SST feedback may be acting to damp the wind stress anomalies and hasten the termination of those first two stages of the event cycle, and prolong the third stage, the southern relaxation. However, the synoptic-scale pressure forcing for the wind stress is also evolving in time [e.g., Mass and Bond, 1996; Nuss, 2007; Fewings *et al.*, 2016], and there are orographic constraints on the wind field [e.g., Rogerson, 1999; Edwards *et al.*, 2002], so SST is not the only influence on wind stress. Evolving synoptic forcing is a known complication in attempts to deduce the role of wind stress-SST coupling in midlatitude locations [Small *et al.*, 2008]. Given the importance of wind relaxations in the CCS for synoptic weather forecasting, in particular for changes in cloudiness [e.g., Iacobellis and Cayan, 2013], which affect human mortality during heat waves [Gershunov *et al.*, 2009], it would be worthwhile to use a fully coupled ocean-atmosphere model to address whether wind stress-SST feedbacks play a strong role during these wind relaxations.

It is well recognized that the southern wind relaxations are associated with dramatically increased cloudiness and coastal fog [e.g., Nuss *et al.*, 2000; Rahn and Parish, 2010; Iacobellis and Cayan, 2013]. The fact that the southern wind relaxations tend to occur after wind intensifications may be an overlooked factor in the onset and persistence of the greater cloudiness during southern than northern wind relaxations. The wind intensifications precondition the surface ocean to be colder than climatology at the onset of southern wind relaxations (Figure 3). The anomalously low SST may influence fog and cloud formation during the subsequent relaxation.

5. Summary and Conclusions

The wind field along the U.S. West Coast exhibits an event cycle spanning ~ 12 days involving a northern and a southern wind relaxation. Northern and southern wind relaxations result in surprisingly different evolution and spatial patterns of SST anomalies in the northeastern Pacific. To determine whether the net surface heat flux is the main driver of the SST anomalies during the wind relaxations, we analyzed net surface heat fluxes from OAFlex and ISCCP during 44 wind relaxations in June–August 2002–2009. During the northern relaxations, the changes in SST are driven mainly by surface heat flux, primarily reduced evaporative cooling. In contrast, during southern wind relaxations, the surface heat flux explains less than 25% of the warming in SST. The surface heat flux anomaly is small during southern wind relaxations as a result of decreased shortwave radiation, which opposes the decrease in evaporative cooling. This decrease in shortwave radiation during southern wind relaxations is due to fog and low marine stratus clouds that form as the marine boundary layer thickens at the onset of the relaxation, triggered by offshore advection of the desert heat low pressure from the southwestern U.S. [e.g., Nuss *et al.*, 2000]. Notably, throughout the southern wind relaxation, although the SST trend is positive a cold SST anomaly persists from the preconditioned cold water caused by the preceding wind intensification. Possibly this contributes to the development of thicker clouds during southern than northern relaxations. After estimating the terms that contribute to the residual in the ML heat budget, we conclude that the warming trend in SST during the southern relaxation is likely from a combination of horizontal advection and reduced Ekman pumping and wind-driven entrainment. To determine the relative importance of these terms would require long time series of vertical profiles

of upper ocean structure with higher temporal resolution than the Argo floats and greater spatial coverage than individual moorings.

The factor determining whether the net surface heat flux is the main driver of SST anomalies during wind relaxations in the CCS is whether there is a strong increase in cloudiness that offsets the reduced latent cooling. There is the potential for wind stress-SST feedback to prolong the third stage of the event cycle, the southern wind relaxation. However, the synoptic atmospheric pressure anomalies may propagate too rapidly, or the influences of coastline orography may be too strong, for the feedback to have as clear an effect as is observed over the open ocean. This feedback possibility and the effect of the preconditioned cold SST on cloud development during southern relaxations should be explored with a fully coupled ocean-atmosphere model of the CCS. Also, due to the effects of coastline shape on the wind field, it would be instructive to carry out similar heat budget analyses for wind relaxations in other eastern boundary upwelling systems.

Acknowledgments

This study was supported by NASA Ocean Vector Winds Science Team Grants NNX10AO94G to UCSB and NNX14AI06G to UConn and NSF grants OCE-1031893 and OCE-1232779. For some plots, we used M_Map by Rich Pawlowicz and JLAB: Lilly, J. M. (2012), JLAB: Matlab freeware for data analysis, Version 0.94, <http://www.jmlilly.net/jmlsoft.html>. Carlos Moffat (University of Delaware) provided some Matlab code. We thank Heather Holbach and Mark Bourassa (FSU) for sharing their Matlab code for calculating wind stress curl and James Edson (UConn), Libe Washburn (UCSB), and two anonymous reviewers for helpful comments on the manuscript. The QuikSCAT L2 Version 3 data are available at http://podaac.jpl.nasa.gov/dataset/QSCAT_LEVEL_2B_OWV_COMP_12, the AMSR-E L2P SST data at <http://podaac.jpl.nasa.gov/dataset/REMS-L2P-AMSR>, the Argo data at <http://mixedlayer.ucsb.edu>, and the OAF flux and ISCCP products on the OAF flux grid at <http://oafux.whoi.edu>.

References

- Bakun, A., and C. S. Nelson (1991), The seasonal cycle of wind-stress curl in subtropical eastern boundary current regions, *J. Phys. Oceanogr.*, *21*(12), 1815–1834, doi:10.1175/1520-0485(1991)021<1815:TSCOWS>2.0.CO;2.
- Bane, J. M., M. D. Levine, R. M. Samelson, S. Haines, M. Meaux, N. Perlin, P. M. Kosro, and T. Boyd (2005), Atmospheric forcing of the Oregon coastal ocean during the 2001 upwelling season, *J. Geophys. Res.*, *110*, C10S02, doi:10.1029/2004JC002653.
- Bane, J. M., Y. H. Spitz, R. M. Letelier, and W. T. Peterson (2007), Jet stream intraseasonal oscillations drive dominant ecosystem variations in Oregon's summertime coastal upwelling system, *Proc. Natl. Acad. Sci. U. S. A.*, *104*(33), 13,262–13,267, doi:10.1073/pnas.0700926104.
- Bond, N. A., C. F. Mass, and J. E. Overland (1996), Coastally trapped wind reversals along the United States west coast during the warm season. Part I: Climatology and temporal evolution, *Mon. Weather Rev.*, *124*(3), 430–445.
- Bourassa, M. A., and K. McBeth Ford (2010), Uncertainty in scatterometer-derived vorticity, *J. Atmos. Oceanic Technol.*, *27*(3), 594–603, doi:10.1175/2009JTECHO689.1.
- Brink, K., R. Beardsley, P. P. Niiler, M. R. Abbott, A. Huyer, S. Ramp, T. Stanton, and D. Stuart (1991), Statistical properties of near surface currents in the California coastal transition zone, *J. Geophys. Res.*, *96*(C8), 14,693–14,706.
- Chelton, D. B., and F. J. Wentz (2005), Global microwave satellite observations of sea surface temperature for numerical weather prediction and climate research, *Bull. Am. Meteorol. Soc.*, *86*(8), 1097–1115, doi:10.1175/BAMS-86-8-1097.
- Chelton, D. B., M. G. Schlax, and R. M. Samelson (2007), Summertime coupling between sea surface temperature and wind stress in the California Current System, *J. Phys. Oceanogr.*, *37*(3), 495–517, doi:10.1175/JPO3025.1.
- Cronin, M., and J. Sprintall (2009), Wind-and buoyancy-forced upper ocean, in *Elements of Physical Oceanography: A Derivative of the Encyclopedia of Ocean Sciences*, edited by J. H. Steele, S. A. Thorpe, and K. K. Turekian, p. 237, Academic, San Diego, Calif.
- Dever, E. P. (2004), Objective maps of near-surface flow states near Point Conception, California, *J. Phys. Oceanogr.*, *34*, 444–461.
- Dudas, S. E., B. A. Grantham, A. R. Kirincich, B. A. Menge, J. Lubchenco, and J. A. Barth (2009), Current reversals as determinants of intertidal recruitment on the central Oregon coast, *ICES J. Mar. Sci.*, *66*(2), 396–407, doi:10.1093/icesjms/fsn179.
- Edson, J. B., V. Jampana, R. A. Weller, S. P. Bigorre, A. J. Plueddemann, C. W. Fairall, S. D. Miller, L. Mahrt, D. Vickers, and H. Hersbach (2013), On the exchange of momentum over the open ocean, *J. Phys. Oceanogr.*, *43*(8), 1589–1610, doi:10.1175/JPO-D-12-0173.1.
- Edwards, K. A., D. P. Rogers, and C. E. Dorman (2002), Adjustment of the marine atmospheric boundary layer to the large-scale bend in the California coast, *J. Geophys. Res.*, *107*(C12), 3213, doi:10.1029/2001JC000807.
- Fairall, C., E. F. Bradley, J. Godfrey, G. Wick, J. B. Edson, and G. Young (1996), Cool-skin and warm-layer effects on sea surface temperature, *J. Geophys. Res.*, *101*(C1), 1295–1308.
- Fawcett, A., G. Pitcher, and F. Shillington (2008), Nearshore currents on the southern Namaqua shelf of the Benguela upwelling system, *Cont. Shelf Res.*, *28*(8), 1026–1039, doi:10.1016/j.csr.2008.02.005.
- Fewings, M. R., L. Washburn, and J. C. Ohlmann (2015), Coastal water circulation patterns around the Northern Channel Islands and Point Conception, California, *Prog. Oceanogr.*, *138*, Part A, 283–304, doi:10.1016/j.pocean.2015.10.001.
- Fewings, M. R., L. Washburn, C. E. Dorman, C. Gotschalk, and K. Lombardo (2016), Synoptic forcing of wind relaxations at Pt. Conception, California, *J. Geophys. Res. Oceans*, *121*, 5711–5730, doi:10.1002/2016JC011699.
- Flynn, K. R. (2016), The causes of regional sea-surface temperature anomalies during wind relaxation events off the U.S. West Coast in summer, Master's thesis, Univ. of Conn., Groton.
- Fore, A. G., B. W. Stiles, A. H. Chau, B. A. Williams, R. S. Dunbar, and E. Rodríguez (2014), Point-wise wind retrieval and ambiguity removal improvements for the QuikSCAT climatological data set, *IEEE Trans. Geosci. Remote Sens.*, *52*(1), 51–59, doi:10.1109/TGRS.2012.2235843.
- Gan, J., and J. S. Allen (2002), A modeling study of shelf circulation off northern California in the region of the Coastal Ocean Dynamics Experiment: Response to relaxation of upwelling winds, *J. Geophys. Res.*, *107*(C9), 3123, doi:10.1029/2000JC000768.
- García-Lafuente, J., J. Delgado, F. Criado-Aldeanueva, M. Bruno, J. del Río, and J. M. Vargas (2006), Water mass circulation on the continental shelf of the Gulf of Cádiz, *Deep Sea Res., Part II*, *53*(11), 1182–1197, doi:10.1016/j.dsr2.2006.04.011.
- Garreaud, R. D., J. A. Rutllant, and H. Fuenzalida (2002), Coastal lows along the subtropical west coast of South America: Mean structure and evolution, *Mon. Weather Rev.*, *130*(1), 75–88.
- Gershunov, A., D. R. Cayan, and S. F. Iacobellis (2009), The great 2006 heat wave over California and Nevada: Signal of an increasing trend, *J. Clim.*, *22*(23), 6181–6203, doi:10.1175/2009JCLI2465.1.
- Halliwel, G. R., and J. S. Allen (1987), The large-scale coastal wind field along the west coast of North America, 1981–1982, *J. Geophys. Res.*, *92*(C2), 1861–1884.
- Harms, S., and C. D. Winant (1998), Characteristic patterns of the circulation in the Santa Barbara Channel, *J. Geophys. Res.*, *103*(C2), 3041–3065, doi:10.1029/97JC02393.
- Hartmann, D. L., M. E. Ockert-Bell, and M. L. Michelsen (1992), The effect of cloud type on Earth's energy balance: Global analysis, *J. Clim.*, *5*(11), 1281–1304, doi:10.1175/1520-0442(1992)005<1281:TEOCTO>2.0.CO;2.
- Hickey, B. M. (1979), The California Current system—Hypotheses and facts, *Prog. Oceanogr.*, *8*(4), 191–279.

- Holbach, H. M., and M. A. Bourassa (2014), The effects of gap-wind-induced vorticity, the monsoon trough, and the ITCZ on east Pacific tropical cyclogenesis, *Mon. Weather Rev.*, *142*(3), 1312–1325, doi:10.1175/MWR-D-13-00218.1.
- Holbach, H. M., and M. A. Bourassa (2017), Platform and across-swath comparison of vorticity spectra from QuikSCAT, ASCAT-A, OSCAT, and ASCAT-B scatterometers, *IEEE J. Select. Top. Appl. Earth Obs. Remote Sens.*, doi:10.1109/JSTARS.2016.2642583, in press.
- Holte, J., and L. Talley (2009), A new algorithm for finding mixed layer depths with applications to Argo data and Subantarctic Mode Water formation, *J. Atmos. Oceanic Technol.*, *26*(9), 1920–1939, doi:10.1175/2009JTECH0543.1.
- Holte, J., J. Gilson, L. Talley, and D. Roemmich (2010), *Argo Mixed Layers*, Scripps Inst. of Oceanogr., San Diego, Calif. [Available at <http://mixedlayer.ucsd.edu/>]
- Iacobellis, S. F., and D. R. Cayan (2013), The variability of California summertime marine stratus: Impacts on surface air temperatures, *J. Geophys. Res. Atmos.*, *118*, 9105–9122, doi:10.1002/jgrd.50652.
- Iles, A. C., T. C. Gouhier, B. A. Menge, J. S. Stewart, A. J. Haupt, and M. C. Lynch (2012), Climate-driven trends and ecological implications of event-scale upwelling in the California Current System, *Global Change Biol.*, *18*(2), 783–796, doi:10.1111/j.1365-2486.2011.02567.
- Kirincich, A. R., and J. A. Barth (2009), Time-varying across-shelf Ekman transport and vertical eddy viscosity on the inner shelf, *J. Phys. Oceanogr.*, *39*(3), 602–620, doi:10.1175/2008JPO3969.1.
- Klein, S. A., and D. L. Hartmann (1993), The seasonal cycle of low stratiform clouds, *J. Clim.*, *6*(8), 1587–1606, doi:10.1175/1520-0442(1993)006 < 1587:TSCOLS > 2.0.CO;2.
- Koraćin, D., J. A. Businger, C. E. Dorman, and J. M. Lewis (2005), Formation, evolution, and dissipation of coastal sea fog, *Boundary Layer Meteorol.*, *117*(3), 447–478, doi:10.1007/s10546-005-2772-5.
- Kosro, P. M. (1987), Structure of the coastal current field off northern California during the Coastal Ocean Dynamics Experiment, *J. Geophys. Res.*, *92*(C2), 1637–1654, doi:10.1029/JC092iC02p01637.
- Kraus, E. B., and J. A. Businger (1994), *Atmosphere-Ocean Interaction*, *Oxford Monogr. Geol. Geophys.*, vol. 27, 2nd ed., Oxford Univ. Press, New York.
- Lynn, R. J., and J. J. Simpson (1987), The California Current System: The seasonal variability of its physical characteristics, *J. Geophys. Res.*, *92*(C12), 12,947–12,966.
- Mass, C. F., and N. A. Bond (1996), Coastally trapped wind reversals along the United States west coast during the warm season. Part II: Synoptic evolution, *Mon. Weather Rev.*, *124*(3), 446–461.
- Melton, C., L. Washburn, and C. Gotschalk (2009), Wind relaxations and poleward flow events in a coastal upwelling system on the central California coast, *J. Geophys. Res.*, *114*, C11016, doi:10.1029/2009JC005397.
- Moisan, J. R., and P. P. Niiler (1998), The seasonal heat budget of the North Pacific: Net heat flux and heat storage rates (1950–1990), *J. Phys. Oceanogr.*, *28*(3), 401–421, doi:10.1175/1520-0485(1998)028 < 0401:TSHBOT > 2.0.CO;2.
- Morgan, S. G., J. L. Fisher, S. T. McAfee, J. L. Largier, and C. M. Halle (2012), Limited recruitment during relaxation events: Larval advection and behavior in an upwelling system, *Limnol. Oceanogr.*, *57*(2), 457–470, doi:10.4319/lo.2012.57.2.0457.
- Nuss, W. A. (2007), Synoptic-scale structure and the character of coastally trapped wind reversals, *Mon. Weather Rev.*, *135*(1), 60–81.
- Nuss, W. A., et al. (2000), Coastally trapped wind reversals: Progress toward understanding, *Bull. Am. Meteorol. Soc.*, *81*(4), 719–743, doi:10.1175/1520-0477(2000)081 < 0719:CTWRPT > 2.3.CO;2.
- Palacios, D., S. Bograd, R. Mendelsohn, and F. Schwing (2004), Long-term and seasonal trends in stratification in the California Current, 1950–1993, *J. Geophys. Res.*, *109*, C10016, doi:10.1029/2004JC002380.
- Paulson, C. A., and J. J. Simpson (1977), Irradiance Measurements in the Upper Ocean, *J. Phys. Oceanogr.*, *7*(6), 952–956.
- Payne, R. E. (1972), Albedo of the sea surface, *J. Atmos. Sci.*, *29*(5), 959–970.
- Perlin, N., R. M. Samelson, and D. B. Chelton (2004), Scatterometer and model wind and wind stress in the Oregon-northern California coastal zone, *Mon. Weather Rev.*, *132*(8), 2110–2129.
- Price, J. F., R. A. Weller, and R. Pinkel (1986), Diurnal cycling: Observations and models of the upper ocean response to diurnal heating, cooling, and wind mixing, *J. Geophys. Res.*, *91*(C7), 8411–8427.
- Rahn, D. A., and T. R. Parish (2010), Cessation of the 22–25 June 2006 coastally trapped wind reversal, *J. Appl. Meteorol. Climatol.*, *49*(7), 1412–1428.
- Relvas, P., and E. D. Barton (2002), Mesoscale patterns in the Cape Sao Vicente (Iberian Peninsula) upwelling region, *J. Geophys. Res.*, *107*(C10), 3164, doi:10.1029/2000JC000456.
- Relvas, P., and E. D. Barton (2005), A separated jet and coastal counterflow during upwelling relaxation off Cape Sao Vicente (Iberian Peninsula), *Cont. Shelf Res.*, *25*(1), 29–49, doi:10.1016/j.csr.2004.09.006.
- Remote Sensing Systems (2004), GHRSSST Level 2P Global Subskin Sea Surface Temperature from the Advanced Microwave Scanning Radiometer - Earth Observing System (AMSR-E) on the NASA Aqua satellite, Ver. 4.0, <https://doi.org/10.5067/GHAMS-2PR01>, PO.DAAC, Pasadena, Calif.
- Reynolds, R. W., T. M. Smith, C. Liu, D. B. Chelton, K. S. Casey, and M. G. Schlax (2007), Daily high-resolution-blended analyses for sea surface temperature, *J. Clim.*, *20*(22), 5473–5496.
- Rogerson, A. (1999), Transcritical flows in the coastal marine atmospheric boundary layer, *J. Atmos. Sci.*, *56*(16), 2761–2779.
- Rossov, W., and Y.-C. Zhang (1995), Calculation of surface and top of atmosphere radiative fluxes from physical quantities based on ISCCP data sets: 2. Validation and first results, *J. Geophys. Res.*, *100*(D1), 1167–1197, doi:10.1029/94JD02746.
- Schiffer, R. A., and W. B. Rossow (1983), The International Satellite Cloud Climatology Project (ISCCP)—The first project of the World Climate Research Programme, *Am. Meteorol. Soc. Bull.*, *64*, 779–784.
- SeaPAC (2013), QuikSCAT Level 2B Ocean Wind Vectors in 12.5km Slice Composites Version 3, <https://doi.org/10.5067/QSX12-L2B01>, PO.DAAC, Pasadena, Calif.
- Send, U., R. C. Beardsley, and C. D. Winant (1987), Relaxation from upwelling in the Coastal Ocean Dynamics Experiment, *J. Geophys. Res.*, *92*(C2), 1683–1698, doi:10.1029/JC092iC02p01683.
- Small, R., S. P. deSzoeke, S. P. Xie, L. O'Neill, H. Seo, Q. Song, P. Cornillon, M. Spall, and S. Minobe (2008), Air–sea interaction over ocean fronts and eddies, *Dyn. Atmos. Oceans*, *45*(3), 274–319, doi:10.1016/j.dynatmoce.2008.01.001.
- Stevenson, J. W., and P. P. Niiler (1983), Upper ocean heat budget during the Hawaii-to-Tahiti shuttle experiment, *J. Phys. Oceanogr.*, *13*(10), 1894–1907, doi:10.1175/1520-0485(1983)013 < 1894:UOHBDT > 2.0.CO;2.
- Strub, P. T., J. M. Mesias, V. Montecino, J. Rutlannt, and S. Salinas (1998), Coastal ocean circulation off western South America: Coastal segment (6E), in *The Sea: Ideas and Observations of Progress in the Study of the Seas*, vol. 11, *The Global Coastal Ocean—Regional Studies and Syntheses*, edited by A. R. Robinson and K. H. Brink, chap. 10, Harvard Univ. Press, Cambridge, Mass.
- Suanda, S. H., et al. (2016), Wind relaxation and a coastal buoyant plume north of Pt. Conception, CA: Observations, simulations, and scalings, *J. Geophys. Res. Oceans*, *121*, 7455–7475, doi:10.1002/2016JC011919.

- Swenson, M. S., and P. P. Niiler (1996), Statistical analysis of the surface circulation of the California Current, *J. Geophys. Res.*, *101*(C10), 22,631–22,645.
- Tang, W., W. T. Liu, and B. W. Stiles (2004), Evaluation of high-resolution ocean surface vector winds measured by QuikSCAT scatterometer in coastal regions, *IEEE Trans. Geosci. Remote Sens.*, *42*(8), 1762–1769.
- Wang, Y., S.-P. Xie, H. Xu, and B. Wang (2004), Regional model simulations of marine boundary layer clouds over the southeast Pacific off South America. Part I: Control experiment, *Mon. Weather Rev.*, *132*(1), 274–296, doi:10.1175/1520-0493(2004)132 < 0274: RMSOMB>2.0.CO;2.
- Washburn, L., M. Fewings, C. Melton, and C. Gotschalk (2011), The propagating response of coastal circulation due to wind relaxations along the central California coast, *J. Geophys. Res.*, *116*, C12028, doi:10.1029/2011JC007502.
- Wentz, F. J., C. Gentemann, D. Smith, and D. Chelton (2000), Satellite measurements of sea surface temperature through clouds, *Science*, *288*(5467), 847–850, doi:10.1126/science.288.5467.847.
- Winant, C. D., E. Dever, and M. Hendershott (2003), Characteristic patterns of shelf circulation at the boundary between central and southern California, *J. Geophys. Res.*, *108*(C2), 3021, doi:10.1029/2001JC001302.
- Wood, R. (2012), Stratocumulus clouds, *Mon. Weather Rev.*, *140*(8), 2373–2423, doi:10.1175/MWR-D-11-00121.1.
- Wood, R., and C. S. Bretherton (2006), On the relationship between stratiform low cloud cover and lower-tropospheric stability, *J. Clim.*, *19*(24), 6425–6432, doi:10.1175/JCLI3988.1.
- Yu, L., and R. A. Weller (2007), Objectively analyzed air-sea heat fluxes for the global ice-free oceans (1981–2005), *Bull. Am. Meteorol. Soc.*, *88*(4), 527–539.
- Yu, L., X. Jin, and R. A. Weller (2008), Multidecade global flux datasets from the Objectively Analyzed Air-sea Fluxes (OAFlux) project: Latent and sensible heat fluxes, ocean evaporation, and related surface meteorological variables, *Tech. Rep. OA-2008-01*, Woods Hole Oceanogr. Inst., Woods Hole, Mass.
- Zhang, Y., W. B. Rossow, A. A. Lacis, V. Oinas, and M. I. Mishchenko (2004), Calculation of radiative fluxes from the surface to top of atmosphere based on ISCCP and other global data sets: Refinements of the radiative transfer model and the input data, *J. Geophys. Res.*, *109*, D19105, doi:10.1029/2003JD004457.